

COMPONENTS' AND MATERIALS' PERFORMANCE FOR ADVANCED SOLAR SUPERCRITICAL CO2 POWERPLANTS

Models of the degradation mechanisms

Deliverable Number 4.3

WP4 Evaluation and models of metal/medium interaction

Date: 8 January 2025

Deliverable type: Report

Dissemination level: Public

Lead participant: VTT





AUTHORS

Name	Organization
Tatu Pinomaa, Liva Freimane, Napat Vajragupta, Abhishek Biswas, Anssi Laukkanen	VTT
Marta Navas, Rebeca Hernandez, Elvira Oñorbe, Marta Serrano	CIEMAT
Florian Lebendig, Dmitry Naumenko	Forschungszentrum Jülich
Ceyhun Oskay, Christoph Grimme, Emma White	DECHEMA

DOCUMENT HISTORY

Version	Date	Change
01	04/12/2024	Initial version uploaded

ABOUT THE PROJECT

COMPASsCO₂ is a 4-year HORIZON2020 project started on 1.11.2020. It is led by the German Aerospace Center (DLR), with eleven additional partners from seven European countries.

COMPASsCO₂ aims to integrate CSP particle systems into highly efficient s-CO₂ Brayton power cycles for electricity production. In COMPASsCO₂, the key component for such an integration, i.e. the particle/s-CO₂ heat exchanger, will be validated in a relevant environment. To reach this goal, the consortium will produce tailored particle and alloy combinations that meet the extreme operating conditions in terms of temperature, pressure, abrasion and hot oxidation/carburization of the heat exchanger tubes and the particles moving around/across them. The proposed innovative CSP s-CO₂ Brayton cycle plants will be flexible, highly efficient, economic and 100% carbon neutral large-scale electricity producers.

The research focus of COMPASsCO2 is on three main technological improvements: development of new particles, development of new metal alloys and development of the heat exchanger section.

DISCLAIMER

This project has received funding from the European Union's Horizon 2020 Research and Innovation Action (RIA) under grant agreement No. **958418.**

The content of this publication reflects only the author's view and not necessary those of the European Commission. The Commission is not responsible for any use that may be made of the information this publication contains.

TABLE OF CONTENTS

List	of F	gures	. 3
List	of T	ables	. 4
List	of A	bbreviations	. 4
1	Abs	tract	. 5
2	Intro	oduction	. 5
3	Bac	kground: high temperature wear in metals due to particle impacts	. 6
4	Mod	deling based Analysis of the degradation mechanisms	. 7
4	.1	Erosion test at ciemat	. 7
4	.2	Erosion-oxidation test at FZJ	. 7
5 lifet		crete element method for modeling particle dynamics in the heat exchanger a estimation	
6	Cali	bration of the lifetime estimation model	16
7	Con	clusions	18
7	'.1	Degradation mechanism analysis	18
7	.2	Lifetime estimation	18
Ref	eren	ces	19

LIST OF FIGURES

Figure 1: Modeling framework to simulate the degradation in CSP heat exchanger tubes consisting of particle impact simulations, detailed particle mechanics modeling, response of the oxide layer, and the heat exchanger tube material
Figure 3: Micromechanical simulations of a representative oxide film microstructures, when left column has a lower volume fraction of porosity, and right column has higher porosity, and
each row correspond to a given compression level.
Figure 4: Backscattered electron images, showing the surface oxide layers after 3000 hour of oxidation in 900 C air (original image from Deliverable D4.1). The red circle and line indicate a characteristic surface asperity radius used for contact mechanics analysis
colors indicate the two particle types, and the spread indicates two particle sizes (1 and 1 mm). (c-d) Radial stress state for different particle sizes and impact velocities, where "rough refers to an impact to an asperity of 20 um radius. (e-f): average tensile stress values as
function of impact velocity, where the high tensile stress values are at 20 um asperities. In a graphs, red color indicates BL 16/30 (state of the art proppant), and blue indicates the nove generation four particles developed in WP2 of COMPASsCO21
Figure 6: Particle simulation geometry
that the velocity due to gravity between each tube row, and deceleration starts slightly before meeting the next tube row, where the colling and collisions to the tubes slow down the particles A steady-state behavior is quickly reached, i.e. the same velocity pattern occurs between each tube row.
Figure 9: Wear in the heat exchanger system during a 13 second simulation, showing (a) fu simulation system, (b) distribution of wear at three tube rows on top side, (c) 95 percentile of wear in each tube colored by tube height coordinate, and (d) zoom-in to the end of the simulation time.
Figure 10: Comparison of force and wear distribution with a looser (left) and denser (right arrangement of tubes. The wear volume decreases quickly for the denser tube arrangement which can be attributed to the decrease of particle velocity.
Figure 11: Calibration of the lifetime estimation model to FZJ wear test (from deliverable D4.2) showing the average wear per tube row (left), wear versus time (middle), and the calibrate wear rate up to the 1000 h experiments
Figure 12: Wear prediction for IN740 for 10 years in terms of the median (typical) and 9: percentile (extreme), calibrated to the experimental wear tests
Figure 13: Wear depth prediction for IN740, Haynes 282, and Cr-superalloy for ten years18

LIST OF TABLES

Es konnten keine Einträge für ein Abbildungsverzeichnis gefunden werden.

LIST OF ABBREVIATIONS

COMPASsCO2	Components' and Materials' Performance for Advanced Solar Supercritical CO2 Power Plants			
CIEMAT	Centro de Investigaciones Energéticas Medioambientales y Tecnológicas (Spain)			
DECHEMA	DECHEMA-Forschungsinstitut (Germany)			
FZJ	Forschungszentrum Jülich (Germany)			
CSP	Concentrated Solar Power (Plants)			
EC	European Commission			
EU	European Union			
H282	Haynes 282			
IN740	INCONEL 740			
IN617	INCONEL 617 (Alloy 617)			
ОМ	Optical Microscopy			
P92	Ferritic steel grade P92			
SEM/EDS	Scanning Electron Microscope/ Energy Dispersive X ray Spectrocopy			
SOTA	Sate Of The Art (Materials)			
SP	Small Punch			
SPC	Small Punch Creep			

1 ABSTRACT

The thermal efficiency of concentrated solar power (CSP) is currently limited by the operating temperatures of state-of-the-art thermal oil or molten salt plants. In the case of innovative particle / supercritical-CO2 CSP plants, higher efficiencies can be reached, but the heat exchanger tubes are exposed to aggressive erosion-corrosion environment at elevated temperatures. In Work Package 4 of the H2020 COMPASsCO2 project, the focus is on understanding, evaluating, and predicting the degradation of the heat exchanger tubes for the considered state-of-the-art and newly developed materials, including the heat carrier particles developed in Work Package 2 and the heat exchanger tube materials developed in Work Package 3.

Based on the extensive Work Package 4 experimental campaigns carried out in Tasks 1 and 2, a modeling-based analysis is performed in Task 3, summarized in this report, Deliverable D4.3. This report provides a comprehensive overview of the degradation mechanisms in the heat exchanger tubes, and it also establishes a framework for lifetime estimation, drawing heavily on the experimental results carried out in this Work Package. The simulation analyses include high-fidelity finite element modelling, analytical contact mechanics, and discrete element method analyses.

2 INTRODUCTION

Work Package 4 of the H2020 COMPASsCO2 project is focused on the evaluation and modelling of metal/medium interactions and the assessment of candidate materials for particle/s-CO₂ heat exchangers. As the primary usage of these materials is in the heat exchanger of the innovative CSP-supercritical CO₂ power plants, a simulation framework for describing the degradation mechanisms of the heat exchanger materials is developed, focusing on the mechanical behavior.

The laboratory tests are carried out under conditions that simulate actual plant conditions. The degradation mechanisms of the materials are analyzed and funneled into a model to predict operating lifetimes of the materials (heat carrier particles and heat exchanger components). Service lifetime estimation models of the interactions between particles degradation, alloys erosion and corrosion are developed. The objectives are:

- To investigate the degradation mechanisms of the candidate materials
- To develop a lifetime estimation model

Task 4.3 focused on investigating the material degradation on the outer side of the heat exchanger tubes using modeling tools. While this report focuses on the modeling work carried out in Task 4.3, it relies heavily on the experimental work carried out in Task 4.1 and Task 4.2. The modeling-based framework is summarized in Figure 1, illustrating the interplay between detailed finite element mechanics based particle impacts, experimental testing, role of oxide layers, and heat exchanger tube material behavior.

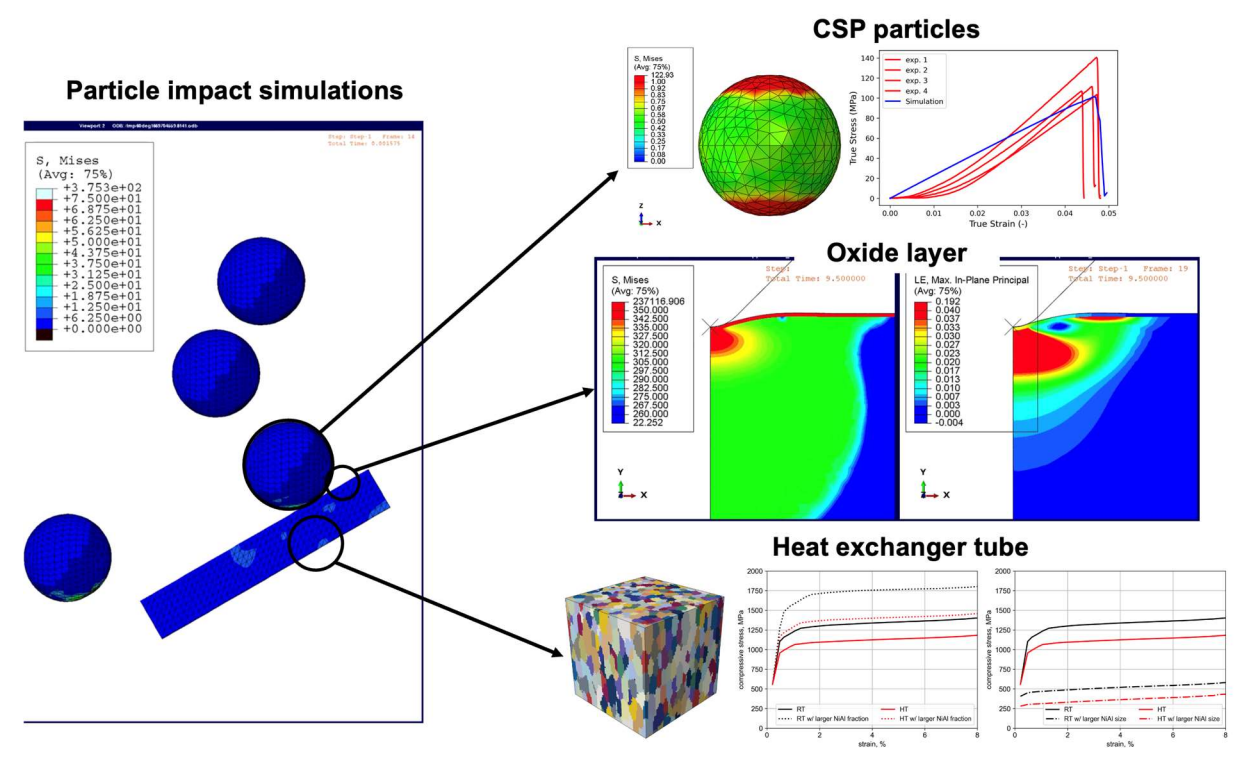


Figure 1: Modeling framework to simulate the degradation in CSP heat exchanger tubes, consisting of particle impact simulations, detailed particle mechanics modeling, response of the oxide layer, and the heat exchanger tube material.

3 BACKGROUND: HIGH TEMPERATURE WEAR IN METALS DUE TO PARTICLE IMPACTS

Particle impacts on metal surfaces result in significant wear, mainly through two mechanisms: **erosion** (Roy, 2006) and **abrasion** (Varga, 2017). Erosion wear occurs when particles strike a metal surface at various angles and velocities, causing material removal through repeated impacts. Abrasion happens when particles slide or roll over the surface, scraping away material. These processes are common in industries with high-speed particles in contact with metal, such as in turbines, pipelines, and mining equipment, leading to reduced durability and efficiency of metal components. We expect that the mechanical wear of the heat exchanger tubes is dominated by abrasive wear mechanism, as the particles are flowing at low speed around the tubes in the operating conditions set in this project.

Erosion Mechanism: Erosion is progressive material loss from repeated particle impacts. Its severity depends on particle size, shape, hardness, impact angle, and velocity:

- Angle of Impact: Impacts at low angles (15-30°) produce more wear in ductile metals, while higher angles (close to 90°) lead to more wear in brittle materials.
- Particle Properties: Hard, sharp particles like sand or minerals cause more severe wear, especially when large or fast-moving.
- Target Material Properties: Softer metals deform under impact, while harder metals resist erosion better.

Abrasion Mechanism: Abrasive wear involves particles sliding along the surface, creating grooves or scratches:

- Two-Body Abrasion: Particles are pressed directly between two surfaces, scoring or plowing through metal.
- Three-Body Abrasion: Particles slide freely, causing less localized but still significant wear.
- Surface Hardness: Abrasion depends on the hardness of the metal relative to particles; softer metals suffer more extensive wear.

Impact of Elevated Temperature: Higher temperatures can worsen wear, as metals soften, reducing hardness and making them more susceptible to particle impacts. In materials like steel, high temperatures weaken microstructures, increasing erosion rates. Some high-temperature alloys resist these effects, retaining hardness under extreme conditions.

Effect of Oxidation: Oxidation is a critical factor in high-temperature wear. Oxide layers can either protect the metal surface or accelerate wear:

- Protective Oxide Layers: Some metals form stable oxides that shield the metal, reducing further erosion or abrasion.
- Brittle Oxide Layers: Brittle oxides can crack and spall under particle impacts, exposing fresh metal and accelerating wear cycles, particularly in metals like iron.

4 MODELING BASED ANALYSIS OF THE DEGRADATION MECHANISMS

In what follows, we carry out a modeling-driven analysis of the degradation of the heat exchanger tubes, based on the experimental investigations carried out previously in Tasks 4.1 and 4.2, to which various simulation techniques are applied to rationalize the results.

4.1 EROSION TEST AT CIEMAT

In the erosion tests carried out by CIEMAT, cylinders were rotated in a container of particles, where the cylinders consisted of state-of-the-art or newly developed heat exchanger materials, and the particles were the state-of-the-art materials. One experiment was performed with Saint-Gobain's bauxite BL16/30 particles, to compare with the newly developed FerOx particles with the same size (590 / 1190 μm). The coatings were tested simultaneously on specimens of P92 and Haynes 282, to study the effect of the coating on metals with FerOx particles. Tests were carried out in air at 700 °C up to 1000 hours with two different rotating speeds corresponding to 5 mm/s and 20 mm/s lineal velocities. Instead of weight loss expected for ideal erosion, the results showed mass gain; based on microstructural analysis, the weight gain seems to be primarily related to deposition of particles on the heat exchanger tube surface, while a secondary effect seems to be oxide scale growth. Due to the mass gain and heavy particle deposition, other experimental data was used to calibrate the modeling approach.

4.2 EROSION-OXIDATION TEST AT FZJ

Three testing facilities were set-up for erosion-oxidation testing at temperatures of 600, 700, and 900 °C in air. The erosion testing was performed in a vertical furnace filled with particles and the specimen holder was rotated at a predefined constant speed. To simulate normal

operating conditions for the particle heat exchanger, the particle velocity was set at 5 mm/s. Additionally, a smaller number of erosion-oxidation testing were performed with a higher particle velocity of 20 mm/s corresponding to maximum possible velocity during plant operation, with more details presented in Deliverable 4.2. For 600 °C and 700 °C, the experimental results indicate minimal mass change when accounting for the oxide film growth. In other words, the oxide films are protective at 600 °C and 700 °C, for typical impact velocities in the operating conditions of 5-20 mm/s. This can be rationalized with a Hertzian contact model, which assumes ideal elastic contact between the particle and oxide film surface. As the deformation depths are below the experimentally observed oxide film thicknesses, we assume that the contact mechanics is dictated by the ceramic particle and the oxide film, which are brittle materials with non-metallic bonding, whose strength is typically limited by the tensile stresses in the material. According to the Hertzian contact model, the only tensile stress states occur at the peripheries of the sphere-plane contact domain (Johnson, 1985); the distribution of these stresses under a 5 mm/s and 20 mm/s impacts are plotted, assuming that all of the impact kinetic energy converts to the elastic mechanical energy. The resulting tensile stress profile is shown in Figure 2, showing that the deformation depths are 1-5 microns at these surfaces.

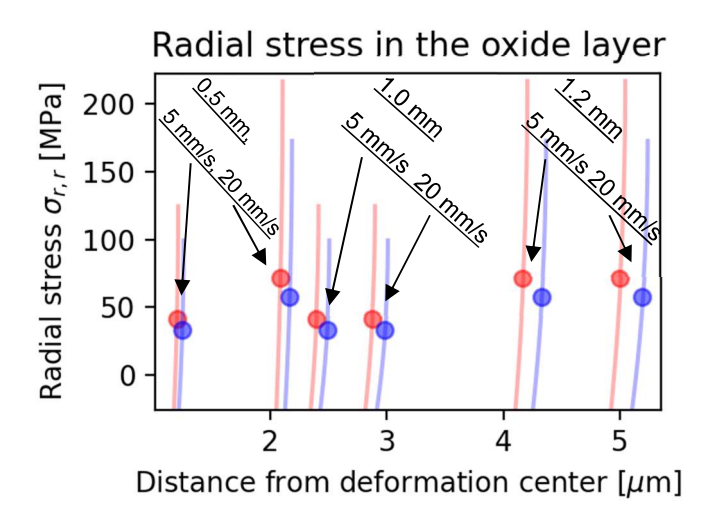


Figure 2: Tensile stresses in a corundum (alumina, Al2O3) oxide layer, showing values below the typical tensile strength of alumina. Red color indicates BL 16/30 (state of the art proppant), and blue indicates the four novel particles developed in WP2 of COMPASsCO2, where the circles indicate the volume-averaged tensile stresses. Three particle diameters are considered: 0.5 mm, 1.0 mm, and 1.2 mm, and two velocities are considered, namely 5 mm/s and 20 mm/s, clustered.

However, as indicated by the experiments at FZJ, the erosion rate increases noticeably at 900 °C for identical particle impact velocities. This is hypothesized to be due to faster and defect-dense oxide films growing at 900 °C compared to 600 °C and 700 °C. Indeed, while the tensile stresses are below 200 MPa and average to approximately 50 MPa in these conditions, the tensile contact stresses can be significantly higher locally if there any microstructural heterogeneities, such as internal pores or large surface roughness or asperities, which often occur due to fast imperfect oxide film growth. These heterogeneities can significantly reduce the critical crack closure stress, i.e. the tensile stress value required to open—not close—a pre-existing microcrack or a new crack. An example of the effect of porosity is shown in Figure 3, showing the difference between a low-porosity (left column) vs. high porosity (right column) oxide microstructure at identical compression levels at different rows; high porosity microstructure leads to higher stress peaks, the middle row shows the microstructures right

before the high porosity microstructure develops a crack, which is shown in the bottom right corner.

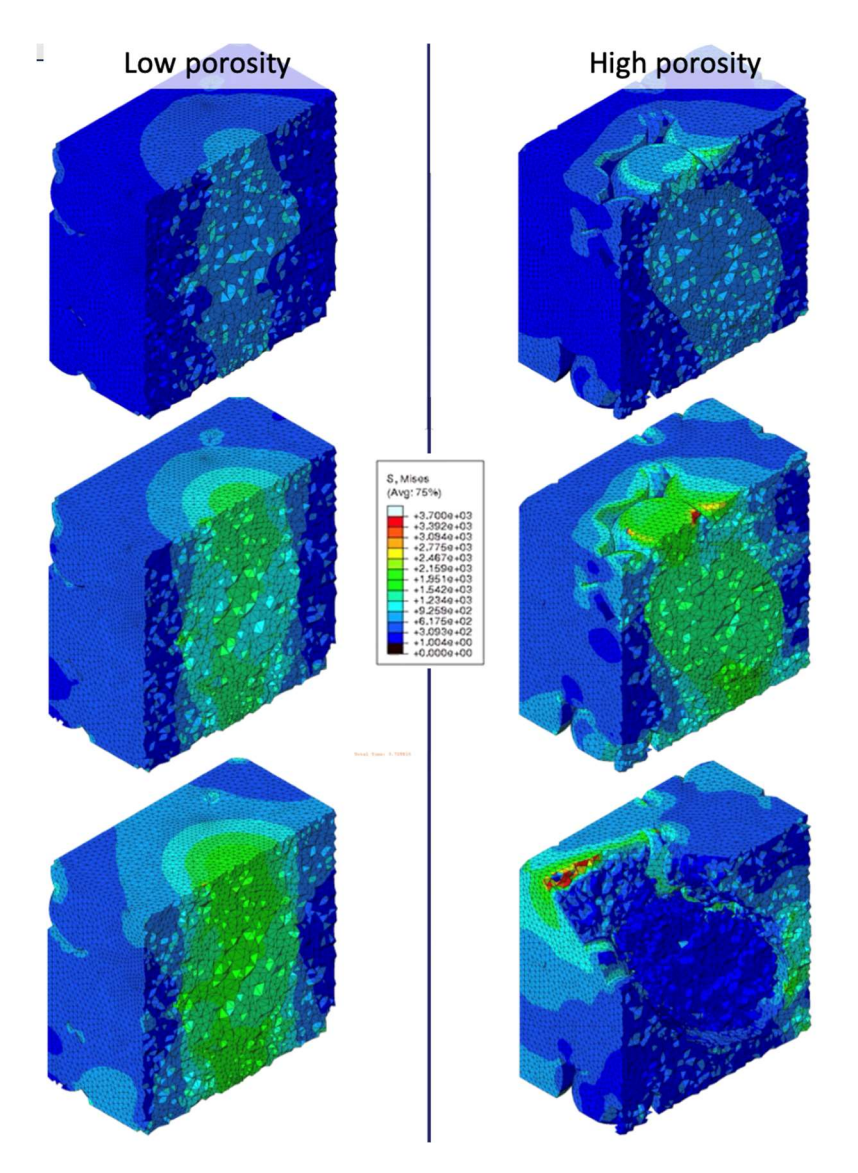
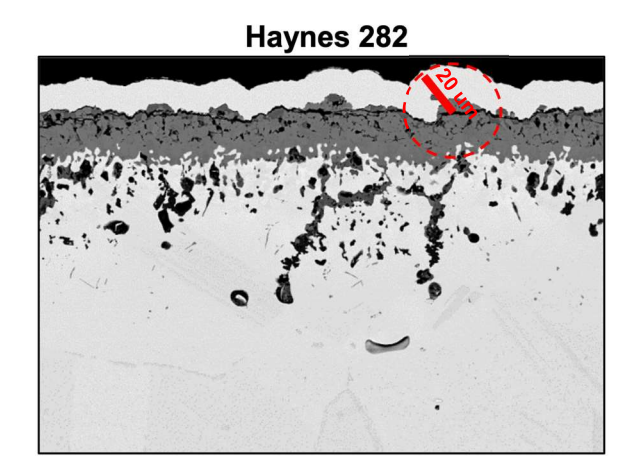


Figure 3: Micromechanical simulations of a representative oxide film microstructures, where left column has a lower volume fraction of porosity, and right column has higher porosity, and each row correspond to a given compression level.

Another source of microstructural heterogeneity is oxide film roughness. Based on experimental images, it is assumed that the oxide film has a characteristic size of approximately 20 microns, estimated from the controlled oxide film analyses in Deliverable D4.1, and the estimation is shown in Figure 4. These types of non-planar asperities are prone to producing stress hot spots.



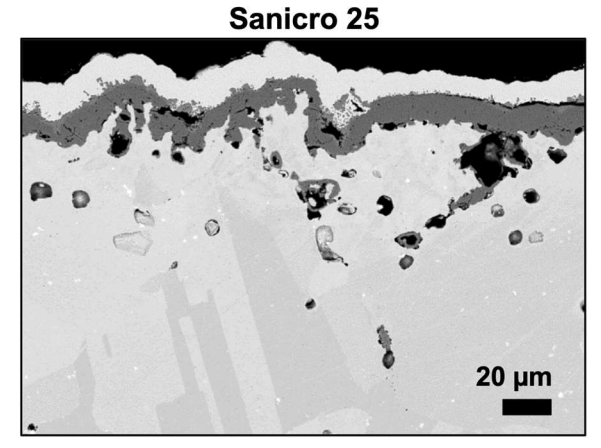


Figure 4: Backscattered electron images, showing the surface oxide layers after 3000 hours of oxidation in 900 C air (original image from Deliverable D4.1). The red circle and line indicate a characteristic surface asperity radius used for contact mechanics analysis.

A more quantitative analysis of this effect based on Hertzian contact mechanics incorporating the effect of asperities was carried out, summarized in Figure 5, where both Al2O3 and Cr2O3 oxide film types are considered. First, the maximum elastic force exerted by the state-of-theart CSP particle (BL 16/30) and a novel generation four (Gen 4) particle are considered, as well as two particle diameters (1 mm and 1.2 mm); additionally, a case where a 1 mm particle impacts head-on to an asperity with radius 20 um (illustrated previously in Figure 4). The results indicate that the asperity leads to significantly higher tensile stresses around the contact, which therefore becomes a likely mechanism of crack initiation in the oxide film. Moreover, these results indicate that between the two considered oxide film types, there is no significant difference in the resulting tensile stresses and the cracking tendency. Note that this does not consider the internal porosity between the two oxide film types, which can differ notably between the two films. Another interesting finding is that the deformation occurs over a relatively small characteristic length scale of 0.1-5 micrometers, which is consistent with the experimental findings in Deliverable D4.2, where it was found that the erosion occurs mostly in the oxide films (and their spallation), and the bulk mechanical properties of the heat exchanger tube material itself seems to have a minor role for the considered impact velocities.

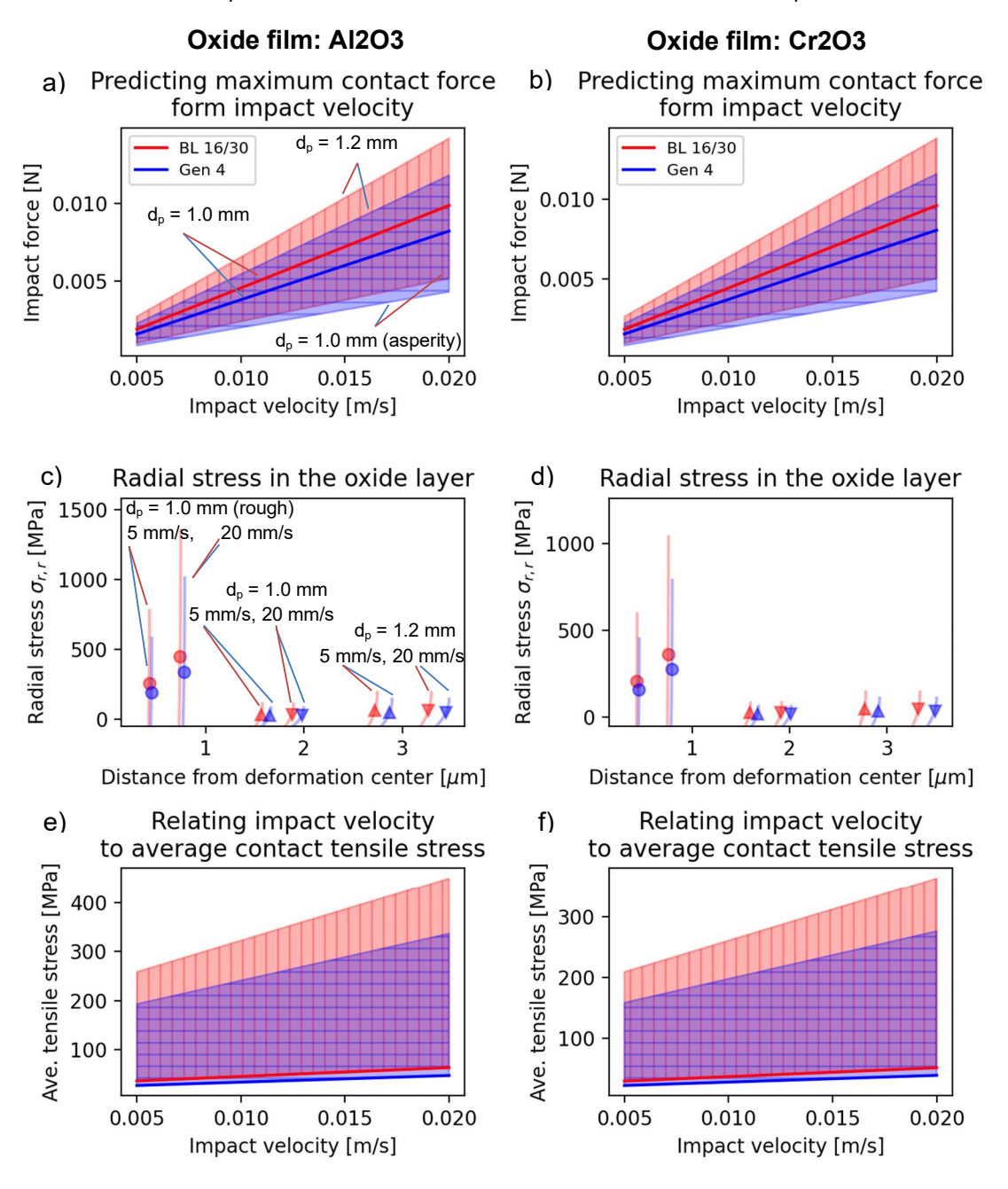


Figure 5: Contact mechanics of Al2O3 and Cr2O3 oxide layers on left and right columns, correspondingly. (a-b) The maximum contact force as a function of impact velocity, where the colors indicate the two particle types, and the spread indicates two particle sizes (1 and 1.2 mm). (c-d) Radial stress state for different particle sizes and impact velocities, where "rough" refers to an impact to an asperity of 20 um radius. (e-f): average tensile stress values as a function of impact velocity, where the high tensile stress values are at 20 um asperities. In all graphs, red color indicates BL 16/30 (state of the art proppant), and blue indicates the novel generation four particles developed in WP2 of COMPASSCO2.

Finally, oxide films can develop notable microstructural stresses due to density changes during the oxide film growths, leading to heterogeneous microstructural stresses, making hot spots of tensile stresses susceptible to crack formation. Note that it is reasonable to assume that the elastic properties of these oxide films do not vary significantly between room temperature and 900 °C (Wang & Fang, 2012).

5 DISCRETE ELEMENT METHOD FOR MODELING PARTICLE DYNAMICS IN THE HEAT EXCHANGER AND LIFETIME ESTIMATION

The backbone of this work is a discrete element method based particle simulation model (Kant & Pitchumani, 2024), which is used to describe the flow of the particles through the heat exchanger tube, and to model the particle collisions on the heat exchanger tube surfaces. The model is based on Lagrangian tracking of particles using an open-source software package called <u>LIGGGHTS</u>. The particle and heat exchanger tube structural material properties (density, size, elastic constants, and hardness) are taken from the literature and the previous deliverables in this project (Deliverables 2.3 and 4.2). The considered geometry is based on the WP5 cold test results, shown in Figure 6a. The distance between the tubes is set so that the horizontal pitch is ten times the particle diameter, i.e. 1 cm.

The representative simulation geometry, shown in Figure 6b, consists of five vertical tube rows, where first, third, and fifth row has two full tubes, and second and fourth row consists of a single full tube in the center, and two halved tubes at the sides; periodic boundary conditions are applied in the vertical directions (along the tube length and along the tube rows), essentially corresponding to infinitely long tubes and infinitely many tubes in each row. Five rows of tubes used as the computational cost increases drastically with the number of tubes considered, and it is feasible to assume that the tubes approach a quasi-steady state behavior as the flow downwards.

A particle diameter of 1 mm was assumed, and the number of particles entering the top part of the system was scaled such that the average mass flow rate per tube top surface area corresponds to the experimental mass flow rate top surface area.

	Density (kg/m³)	Young's modulus (GPa)	Poisson's ratio	Yield strength (MPa)
BL 16/30 particles	3500	319	0.20	-
Gen 4 particles	3300	184	0.15	-
P92 steel	7800	200	0.29	450
Cr-superalloy	7200	279	0.21	700

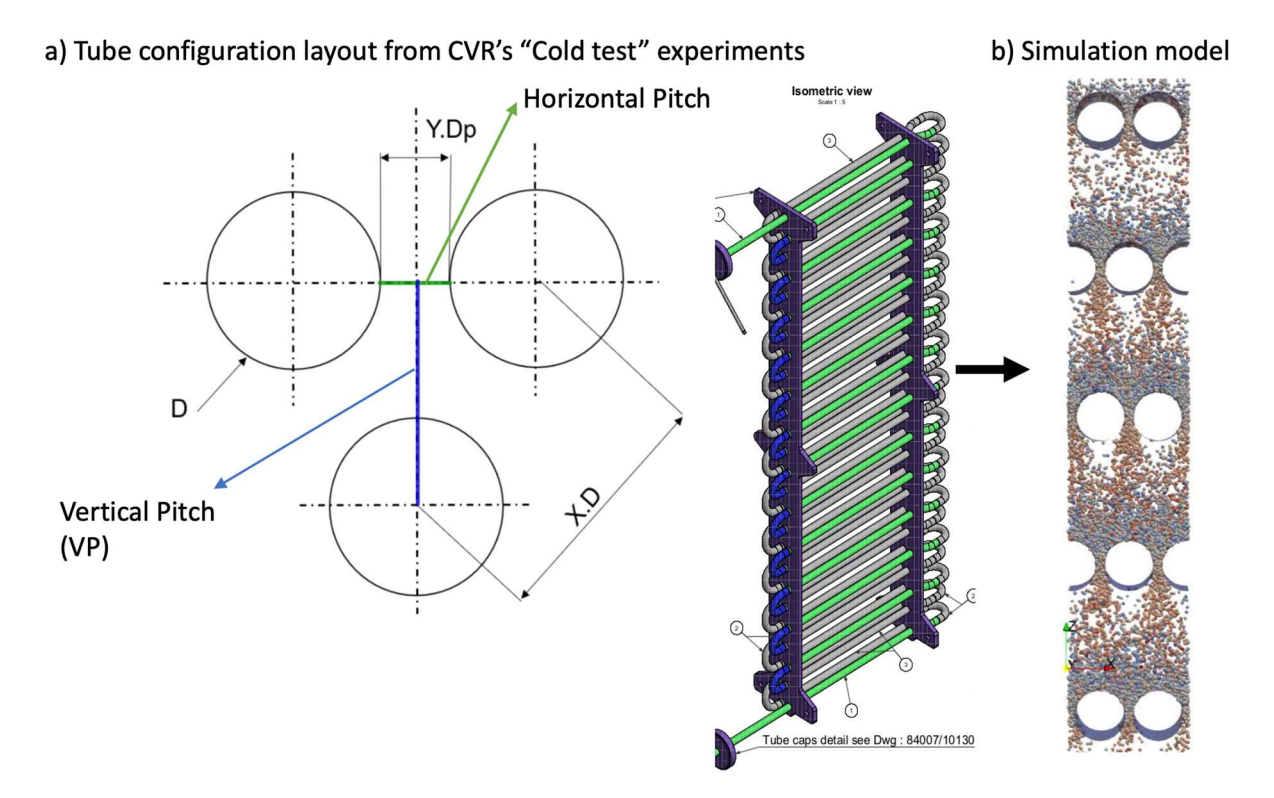


Figure 6: Particle simulation geometry.

The particle impacts are described by a Hertzian contact model, which assumes idealized elastic contact between the particle and the surface, without any off the impact energy being consumed by plastic dissipation. The contact force as a function of time for a single impact is shown in Figure 7 (top), showing that the force obtains a maximum value upon impact, and is reflected with a corresponding force profile away from the surface. The time step size needs to be sufficiently small to smoothly resolve this force profile.

The material wear is described using a Finnie wear model, which assumes that the wear occurs through small incremental removal of material due to impact at an angle, as described by Hertzian contact model of particle-surface interaction. The wear is assumed to accumulate during a single impact before the elastic recoil of the particle starts to move the particle away from the impact surface, i.e. only during the first half of the cumulative wear; the cumulative wear volume during a single impact is shown for a single impact event in in Figure 7 (bottom). It should be noted that the wear volume should be considered a relative quantity at this point, which should be calibrated to experiments.

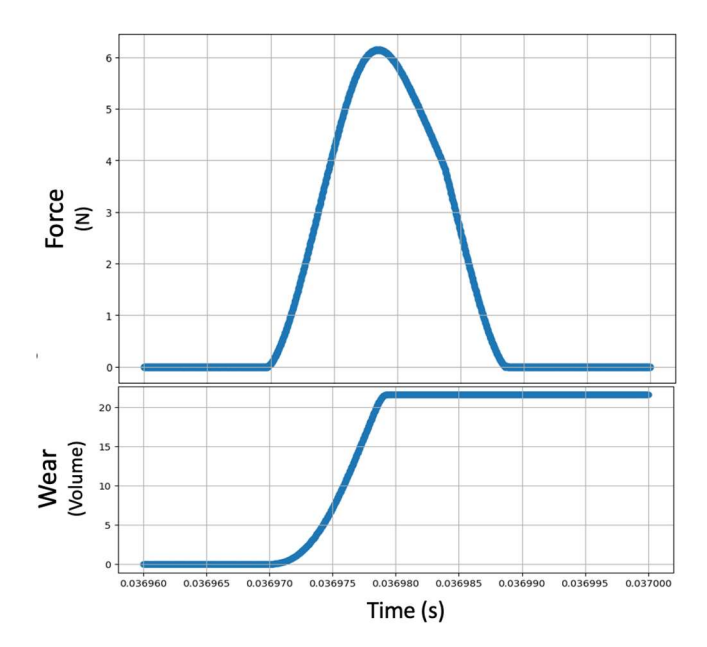


Figure 7: Example of a single particle impact: (top) the force profile according to a Hertzian contact model, (bottom) cumulative wear volume according to the Finnie wear model.

The average velocity as a function of height in the heat exchanger section is shown in Figure 8. The velocity due to gravity between each tube row, and deceleration starts slightly before meeting the next tube row, where the colling and collisions to the tubes slow down the particles. A steady-state behavior is quickly reached, i.e. the same velocity pattern occurs between each tube row.

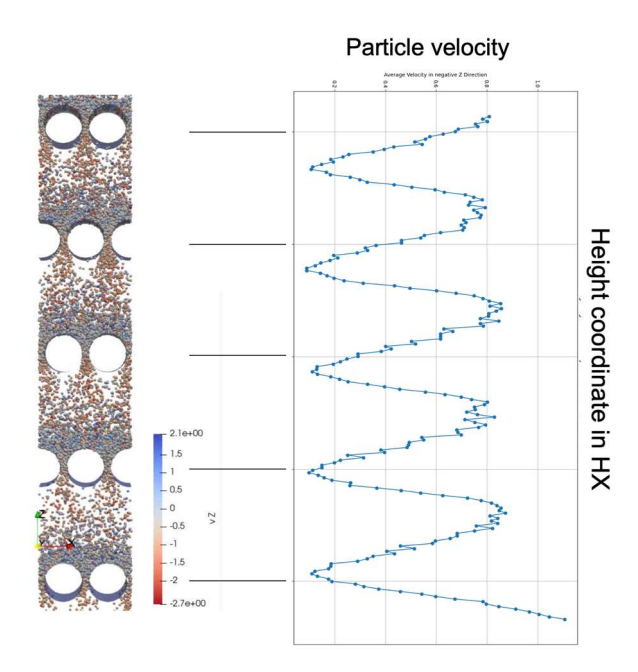


Figure 8: Particle velocity as a function of height in the heat exchanger system. It can be seen that the velocity due to gravity between each tube row, and deceleration starts slightly before meeting the next tube row, where the colling and collisions to the tubes slow down the particles. A steady-state behavior is quickly reached, i.e. the same velocity pattern occurs between each tube row.

The Lagrangian particle simulations discussed in this section have a high computational cost. This is due to the large number of particles in the simulation box to have a representative geometrical section of the full heat exchanger domain. In addition, to fully resolve the Hertzian contact events in time, the simulations are restricted to a relatively small time step. With the current set-up, a typical simulation runs approximately one week, using 120 processors on a supercomputer. Following key measures in the simulations, such as the velocity distributions and local wear rate, we believe that approximately 10 seconds are needed to reach a representative "steady-state" flow condition in the simulated heat exchanger; longer simulation times show a rather linear increase in the wear volume and particle velocity distributions, with stochastic fluctuations visible.

The wear in the simulation system during a 13.5 second simulation is shown in Figure 9. The wear tends to accumulate to the tube top diagonals and not in the tube top center (zenith). The wear is stochastically distributed on the tube surface based on the particle impacts, so there is a rugged distribution of wear accumulating to the tube surface; the 95 percentile of the wear volumes are shown in Figure 9 c, where each line is colored by their tube height coordinate: yellow lines are at the top and therefore start to experience wear before the bottom row of tubes (dark blue). The wear rate (wear volume per time) is very similar for each tube surface, and the differences are roughly due to the distances from the tube surface. The wear starts to reach a steady-state regime after approximately 6 seconds. In Figure 9 d, the zoom-in is shown for the cumulative wear volume; as expected, the wear lowest in the bottom level tube arrays, which have experienced the least amount of particle impacts during a continuous particle flow simulation. Moreover, the dashed lines show the left-side tubes, and solid lines are the right-side tubes, showing that the difference between the sides are negligible.

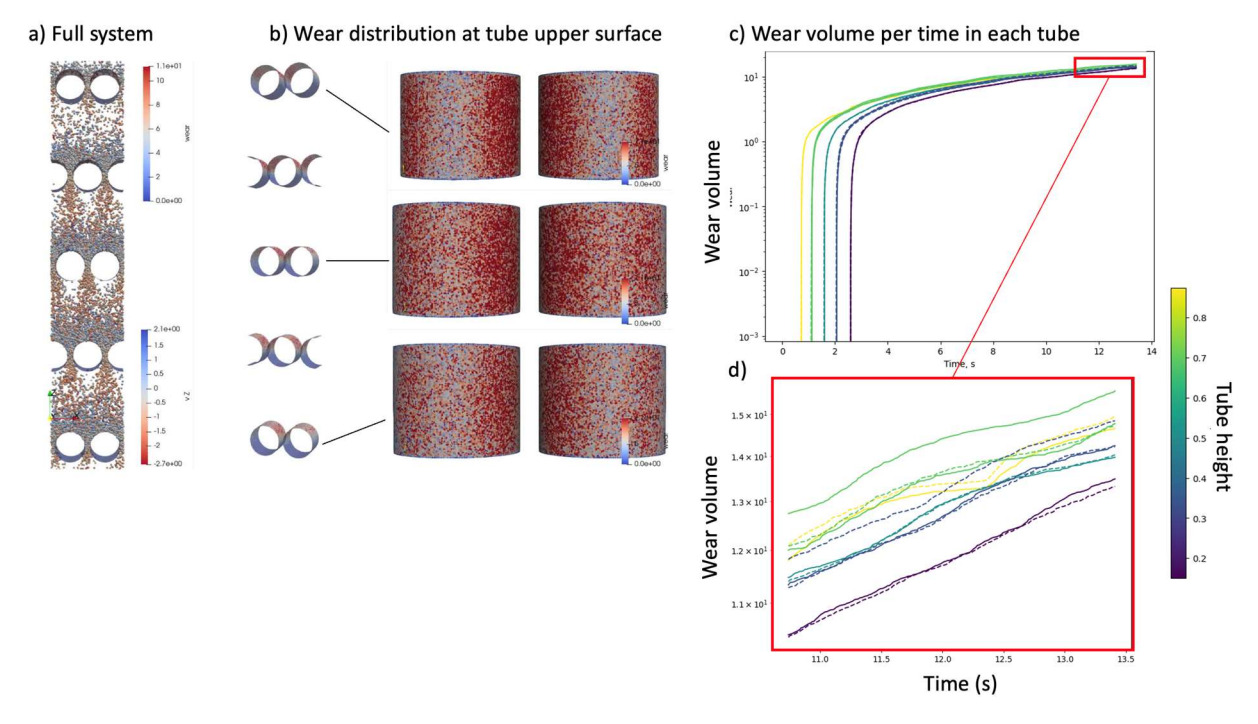


Figure 9: Wear in the heat exchanger system during a 13 second simulation, showing (a) full simulation system, (b) distribution of wear at three tube rows on top side, (c) 95 percentile of wear in each tube colored by tube height coordinate, and (d) zoom-in to the end of the simulation time.

The comparison between two different vertical pitch to tube diameter ratios are considered in Figure 10, where the left side is the reference case, and right side is a denser tube set-up; the

bottom panels show the tube geometry, distribution of particles and wear, and the top panels show the force and wear per tube row. For the denser tube set-up (right side), the forces are orders of magnitude smaller, and importantly, the wear is high on the upper-most tube arrays, after which the particle flow slows down considerably, leading to lower wear volumes; for the reference case (left-side set-up), the wear volume also decreases, but to a lesser degree.

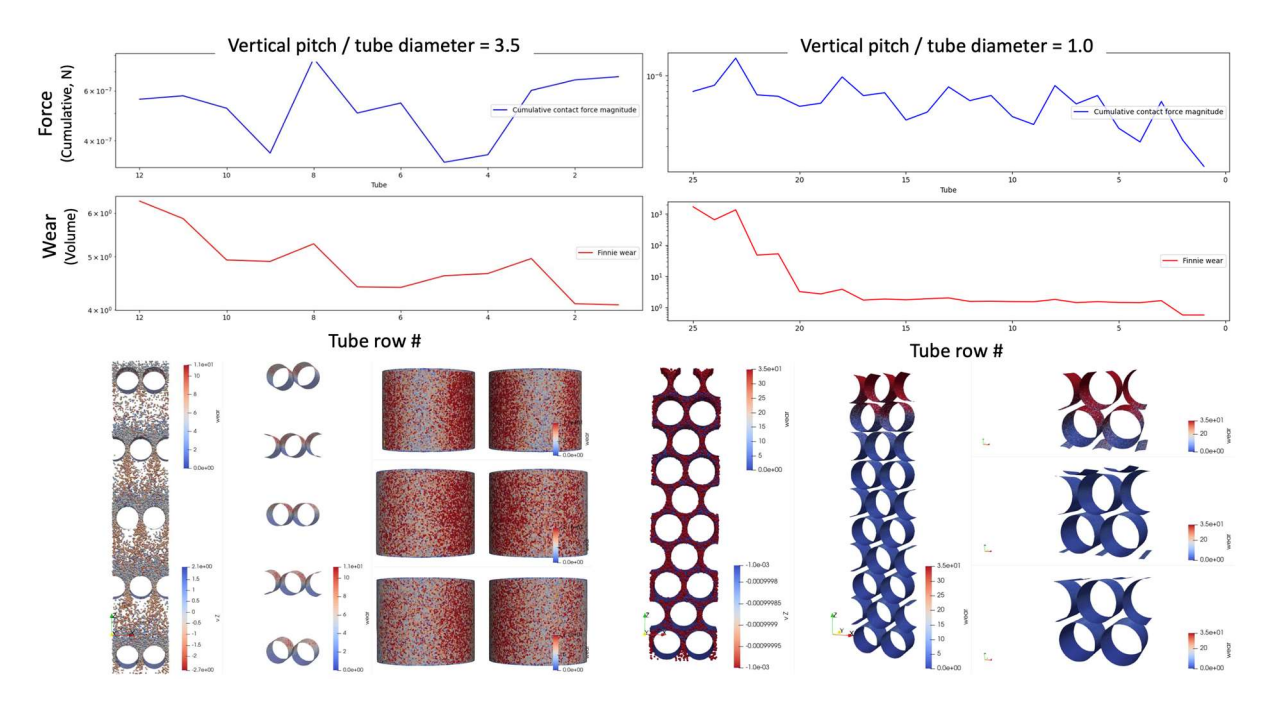


Figure 10: Comparison of force and wear distribution with a looser (left) and denser (right) arrangement of tubes. The wear volume decreases quickly for the denser tube arrangement, which can be attributed to the decrease of particle velocity.

It should be noted that at this point, only the relative wear volumes should be considered; the absolute wear volume comparison require calibration to experiments, which will be carried out as follows.

6 CALIBRATION OF THE LIFETIME ESTIMATION MODEL

In the erosion-oxidation wear tests carried out by FZJ (Deliverable D4.2), it was concluded that the wear occurred exclusively on the oxide films. Therefore, our subsequent analysis focuses on the wear in the oxide films. For now, we exclude the Sanicro 25 analysis, where particle deposition occurs, as this complicates the analysis notably. Based on the 1000 h tests, the linearized average wear rate for IN740 is (5.4-1.6) mg/cm² / 800 h ~ 0.520 g/m² / year. Assuming IN740 density of 8.05e3 kg/m³, the cumulative wear in 10 years is approximately 0.52 mm; in COMPASsCO2, the heat exchanger tube thickness is ~ 2.5 mm; this implies that on average, 20% of the full tube thickness, which also means that, considering the potential localization of plastic deformation, cracking, and wear, it is very likely that locally a structural failure occurs in the tubes during a 10 year lifespan. We calibrate the lifetime estimation model to the IN740 wear volume, and the resulting wear evolution is shown in Figure 11, where the first two panels show the wear versus time versus tube array row number (#) in the discrete element simulations of wear. Linear fit is performed for the quasi-steady state wear accumulation, starting from ~ 5 seconds to the end of the simulation, i.e. 13.5 seconds, as shown in Figure 11 (middle panel). The same wear accumulation is expected to occur over time, and the accumulated wear is calibrated to the FZJ IN740 wear test after 1000 hours (right panel in Figure 11). By using the IN740 density, the accumulated wear (kg/m²) was converted to wear depth (mm).

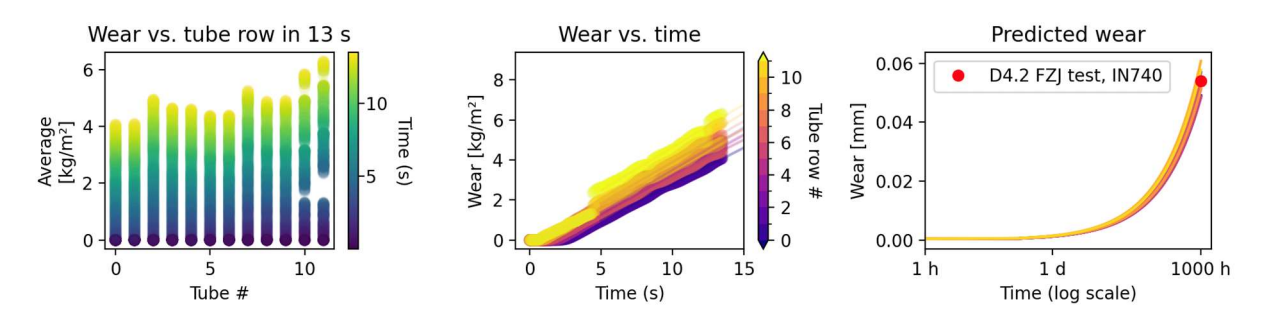


Figure 11: Calibration of the lifetime estimation model to FZJ wear test (from deliverable D4.2), showing the average wear per tube row (left), wear versus time (middle), and the calibrated wear rate up to the 1000 h experiments.

One advantage of discrete element simulations is that statistics of the wear can be obtained. In this case, for the accumulated wear, the focus is on the median (typical value) and 95 percentile, shown as their own rows in Figure 12. Interestingly, the median varies much more than the extreme, indicating that the behavior is more predictable, as it is likely that the extreme events are what lead to localization of deformation and potential catastrophic failure.

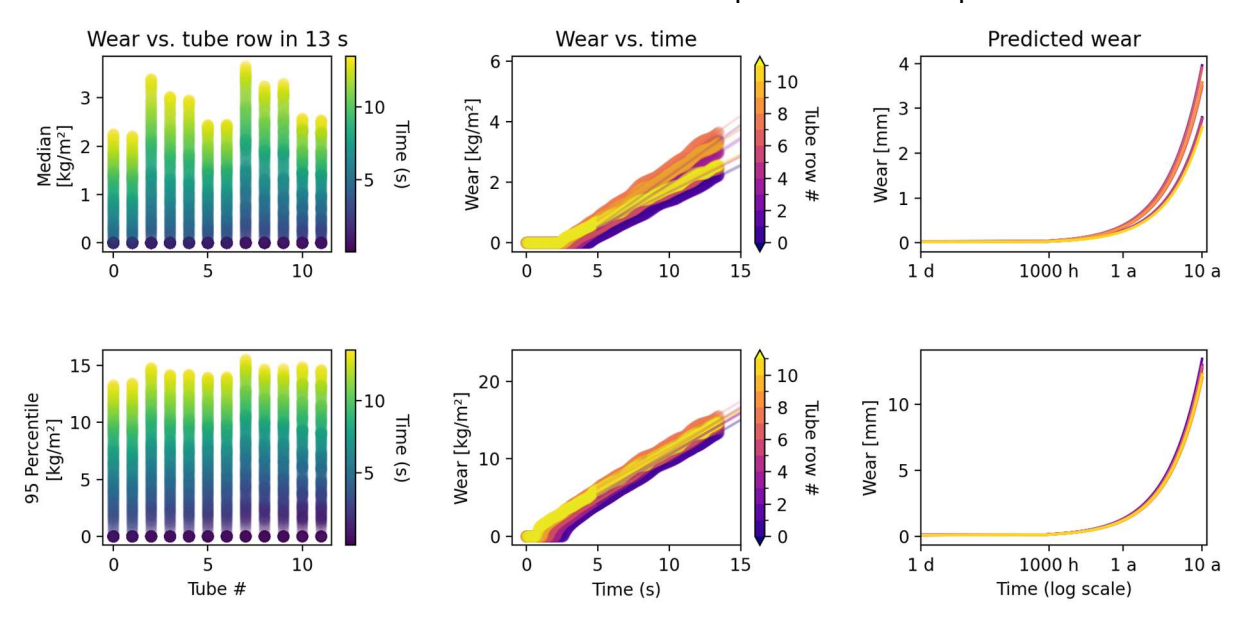


Figure 12: Wear prediction for IN740 for 10 years in terms of the median (typical) and 95 percentile (extreme), calibrated to the experimental wear tests.

Finally, Figure 13 shows the wear depth after 10 years of operation in IN740, Haynes 282, and Cr-superalloy, as predicted by the modeling approach. This shows that the wear in IN740 and Haynes 282 are very similar, whereas the Cr-superalloy shows a slightly higher wear volume. It should be noted that for conclusive results, more careful wear tests should be carried out for Cr-superalloy, which is expected to behave in a qualitatively different manner compared to the superalloys (Ma, 2023).

Figure 13: Wear depth prediction for IN740, Haynes 282, and Cr-superalloy for ten years.

7 CONCLUSIONS

The modeling-based analysis is applied to the heat exchanger tube materials to better understand and predict the degradation behavior. The main conclusions are as follows.

7.1 DEGRADATION MECHANISM ANALYSIS

The contact mechanics modeling verifies that once an oxide layer forms, the particle contact and the associated stress-strain distribution is highly localized within several micrometers area, verifying that indeed, the particles are likely interact mostly with the small-scale oxide layers present on the heat exchanger material surfaces, which are known to form relatively quickly based on the D4.1 and D4.2 experiments. This conclusion supports the experimental findings of FZJ D4.2 erosion-corrosion tests, which suggests that the wear occurs mainly as detachment or spallation of the corrosion layers. Moreover, due to the brittle nature of the particles and the corrosion oxide layers, it is highly unlikely that the facture initiates due to an ideal spherical contact between the proppant and the corrosion oxide surface; instead, any heterogeneities, likely surface asperities or internal pores, are likely to initiate the fracture. Our results also indicate that the fracture initiation does not differ significantly across different particles or corrosion oxide chemistries in terms of their bulk material properties; however, the porosity and surface morphology of the oxide layers and the particles are likely to determine how large tensile stresses emerge in the contact region. A more detailed analysis of the oxide layer contact mechanics would require careful nanoindentation testing, and 3D tomographic imaging of the oxide microstructures to reveal their pore structures, as well as the statistics of their surface asperities.

7.2 LIFETIME ESTIMATION

A major effort in Task 3 was the establishment of a discrete element method-based particle simulation framework, which allowed us to simulate the particle flow in the heat exchanger tube arrangement, and importantly, evaluation of the contact forces and wear volumes using a phenomenological Finnie wear model. This approach allows us to identify that in the heat exchanger surface, detrimental collisions are most likely to occur at the top, but not in the middle of the tube upper surface, but closer to the sides. We can also analyze the statistics of the collisions; in this case, we considered the median (typical) and 95 percentile (extreme) accumulated wear. Our simulations indicate that the median wear varies significantly across notably, roughly 20-40 %, between tube arrays, whereas the extreme collision events are more uniformly distributed between the tube arrays. Due to the high complexity of the wear and corrosion at elevated temperatures in operating conditions, we calibrated the lifetime

estimation model to experimental data performed by FZJ in D4.2, to extrapolate the lifetime of the tubes up to ten years of service.

REFERENCES

- Johnson, K. (1985). Contact Mechanics. Cambridge University Press.
- Kant, & Pitchumani. (2024). Erosion wear analysis of heat exchange surfaces in a falling particle-based concentrating solar power system. *Solar Energy Materials and Solar Cells*, 112629.
- Ma, K. (2023). Chromium-based bcc-superalloys strengthened by iron supplements. *Acta materialia*, 119183.
- Roy, M. (2006). Elevated temperature erosive wear of metallic materials. *Journal of Physics D: Applied Physics*, 39 (101).
- Varga. (2017). High temperature abrasive wear of metallic materials. Wear, 443-451 (15).
- Wang, Y., & Fang, H. (2012). First-principles lattice dynamics, thermodynamics, and elasticity of Cr2O3. *Surface Science*, 1422-1425.

AUTHORS

Name	Organization
Tatu Pinomaa, Liva Freimane, Napat Vajragupta, Abhishek Biswas, Anssi Laukkanen	VTT
Marta Navas, Rebeca Hernandez, Elvira Oñorbe, Marta Serrano	CIEMAT
Florian Lebendig, Dmitry Naumenko	Forschungszentrum Jülich
Ceyhun Oskay, Christoph Grimme, Emma White	DECHEMA

DOCUMENT HISTORY

Version	Date	Change
01	08/01/2025	Initial version uploaded

ABOUT THE PROJECT

COMPASsCO₂ is a 4-year HORIZON2020 project started on 1.11.2020. It is led by the German Aerospace Center (DLR), with eleven additional partners from seven European countries.

COMPASsCO₂ aims to integrate CSP particle systems into highly efficient s-CO₂ Brayton power cycles for electricity production. In COMPASsCO₂, the key component for such an integration, i.e. the particle/s-CO₂ heat exchanger, will be validated in a relevant environment. To reach this goal, the consortium will produce tailored particle and alloy combinations that meet the extreme operating conditions in terms of temperature, pressure, abrasion and hot oxidation/carburization of the heat exchanger tubes and the particles moving around/across them. The proposed innovative CSP s-CO₂ Brayton cycle plants will be flexible, highly efficient, economic and 100% carbon neutral large-scale electricity producers.

The research focus of COMPASsCO2 is on three main technological improvements: development of new particles, development of new metal alloys and development of the heat exchanger section.

DISCLAIMER

This project has received funding from the European Union's Horizon 2020 Research and Innovation Action (RIA) under grant agreement No. **958418.**

The content of this publication reflects only the author's view and not necessary those of the European Commission. The Commission is not responsible for any use that may be made of the information this publication contains.

TABLE OF CONTENTS

List	t of F	igures	3
List	t of T	ables	4
List	t of A	bbreviations	4
1	Abs	tract	5
2	Intro	oduction	5
3	Bac	kground: high temperature wear in metals due to particle impacts	6
4	Mod	deling based Analysis of the degradation mechanisms	7
4	.1	Erosion test at ciemat	7
4	.2	Erosion-oxidation test at FZJ	7
5 lifet		crete element method for modeling particle dynamics in the heat exchanger a	
6	Cali	bration of the lifetime estimation model	.16
7	Cor	nclusions	.18
7	'.1	Degradation mechanism analysis	.18
7	'.2	Lifetime estimation	.18
Ref	feren	ces	.19

LIST OF FIGURES

Figure 1: Modeling framework to simulate the degradation in CSP heat exchanger tubes,
consisting of particle impact simulations, detailed particle mechanics modeling, response of
the oxide layer, and the heat exchanger tube material 6
Figure 2: Tensile stresses in a corundum (alumina, Al2O3) oxide layer, showing values below
the typical tensile strength of alumina. Red color indicates BL 16/30 (state of the art proppant),
and blue indicates the four novel particles developed in WP2 of COMPASsCO2, where the
circles indicate the volume-averaged tensile stresses. Three particle diameters are considered:
0.5 mm, 1.0 mm, and 1.2 mm, and two velocities are considered, namely 5 mm/s and 20 mm/s,
clustered
Figure 3: Micromechanical simulations of a representative oxide film microstructures, where
left column has a lower volume fraction of porosity, and right column has higher porosity, and
each row correspond to a given compression level
Figure 4: Backscattered electron images, showing the surface oxide layers after 3000 hours
of oxidation in 900 C air (original image from Deliverable D4.1). The red circle and line indicate
a characteristic surface asperity radius used for contact mechanics analysis
Figure 5: Contact mechanics of Al2O3 and Cr2O3 oxide layers on left and right columns,
correspondingly. (a-b) The maximum contact force as a function of impact velocity, where the
colors indicate the two particle types, and the spread indicates two particle sizes (1 and 1.2
mm). (c-d) Radial stress state for different particle sizes and impact velocities, where "rough"
refers to an impact to an asperity of 20 um radius. (e-f): average tensile stress values as a
function of impact velocity, where the high tensile stress values are at 20 um asperities. In all
graphs, red color indicates BL 16/30 (state of the art proppant), and blue indicates the novel
generation four particles developed in WP2 of COMPASsCO211
Figure 6: Particle simulation geometry13
Figure 7: Example of a single particle impact: (top) the force profile according to a Hertzian
contact model, (bottom) cumulative wear volume according to the Finnie wear model14
Figure 8: Particle velocity as a function of height in the heat exchanger system. It can be seen
that the velocity due to gravity between each tube row, and deceleration starts slightly before
meeting the next tube row, where the colling and collisions to the tubes slow down the particles.
A steady-state behavior is quickly reached, i.e. the same velocity pattern occurs between each
tube row14
Figure 9: Wear in the heat exchanger system during a 13 second simulation, showing (a) full
simulation system, (b) distribution of wear at three tube rows on top side, (c) 95 percentile of
wear in each tube colored by tube height coordinate, and (d) zoom-in to the end of the
simulation time15
Figure 10: Comparison of force and wear distribution with a looser (left) and denser (right)
arrangement of tubes. The wear volume decreases quickly for the denser tube arrangement,
which can be attributed to the decrease of particle velocity.
Figure 11: Calibration of the lifetime estimation model to FZJ wear test (from deliverable D4.2),
showing the average wear per tube row (left), wear versus time (middle), and the calibrated
wear rate up to the 1000 h experiments
Figure 12: Wear prediction for IN740 for 10 years in terms of the median (typical) and 95
percentile (extreme), calibrated to the experimental wear tests
Figure 13: Wear depth prediction for IN740, Haynes 282, and Cr-superalloy for ten years18

LIST OF TABLES

Es konnten keine Einträge für ein Abbildungsverzeichnis gefunden werden.

LIST OF ABBREVIATIONS

COMPASsCO2	Components' and Materials' Performance for Advanced Solar Supercritical CO2 Power Plants			
CIEMAT	Centro de Investigaciones Energéticas Medioambientales y Tecnológicas (Spain)			
DECHEMA	DECHEMA-Forschungsinstitut (Germany)			
FZJ	Forschungszentrum Jülich (Germany)			
CSP	Concentrated Solar Power (Plants)			
EC	European Commission			
EU	European Union			
H282	Haynes 282			
IN740	INCONEL 740			
IN617	INCONEL 617 (Alloy 617)			
ОМ	Optical Microscopy			
P92	Ferritic steel grade P92			
SEM/EDS	Scanning Electron Microscope/ Energy Dispersive X ray Spectrocopy			
SOTA	Sate Of The Art (Materials)			
SP	Small Punch			
SPC	Small Punch Creep			

1 ABSTRACT

The thermal efficiency of concentrated solar power (CSP) is currently limited by the operating temperatures of state-of-the-art thermal oil or molten salt plants. In the case of innovative particle / supercritical-CO2 CSP plants, higher efficiencies can be reached, but the heat exchanger tubes are exposed to aggressive erosion-corrosion environment at elevated temperatures. In Work Package 4 of the H2020 COMPASsCO2 project, the focus is on understanding, evaluating, and predicting the degradation of the heat exchanger tubes for the considered state-of-the-art and newly developed materials, including the heat carrier particles developed in Work Package 2 and the heat exchanger tube materials developed in Work Package 3.

Based on the extensive Work Package 4 experimental campaigns carried out in Tasks 1 and 2, a modeling-based analysis is performed in Task 3, summarized in this report, Deliverable D4.3. This report provides a comprehensive overview of the degradation mechanisms in the heat exchanger tubes, and it also establishes a framework for lifetime estimation, drawing heavily on the experimental results carried out in this Work Package. The simulation analyses include high-fidelity finite element modelling, analytical contact mechanics, and discrete element method analyses.

2 INTRODUCTION

Work Package 4 of the H2020 COMPASsCO2 project is focused on the evaluation and modelling of metal/medium interactions and the assessment of candidate materials for particle/s-CO₂ heat exchangers. As the primary usage of these materials is in the heat exchanger of the innovative CSP-supercritical CO₂ power plants, a simulation framework for describing the degradation mechanisms of the heat exchanger materials is developed, focusing on the mechanical behavior.

The laboratory tests are carried out under conditions that simulate actual plant conditions. The degradation mechanisms of the materials are analyzed and funneled into a model to predict operating lifetimes of the materials (heat carrier particles and heat exchanger components). Service lifetime estimation models of the interactions between particles degradation, alloys erosion and corrosion are developed. The objectives are:

- To investigate the degradation mechanisms of the candidate materials
- To develop a lifetime estimation model

Task 4.3 focused on investigating the material degradation on the outer side of the heat exchanger tubes using modeling tools. While this report focuses on the modeling work carried out in Task 4.3, it relies heavily on the experimental work carried out in Task 4.1 and Task 4.2. The modeling-based framework is summarized in Figure 1, illustrating the interplay between detailed finite element mechanics based particle impacts, experimental testing, role of oxide layers, and heat exchanger tube material behavior.

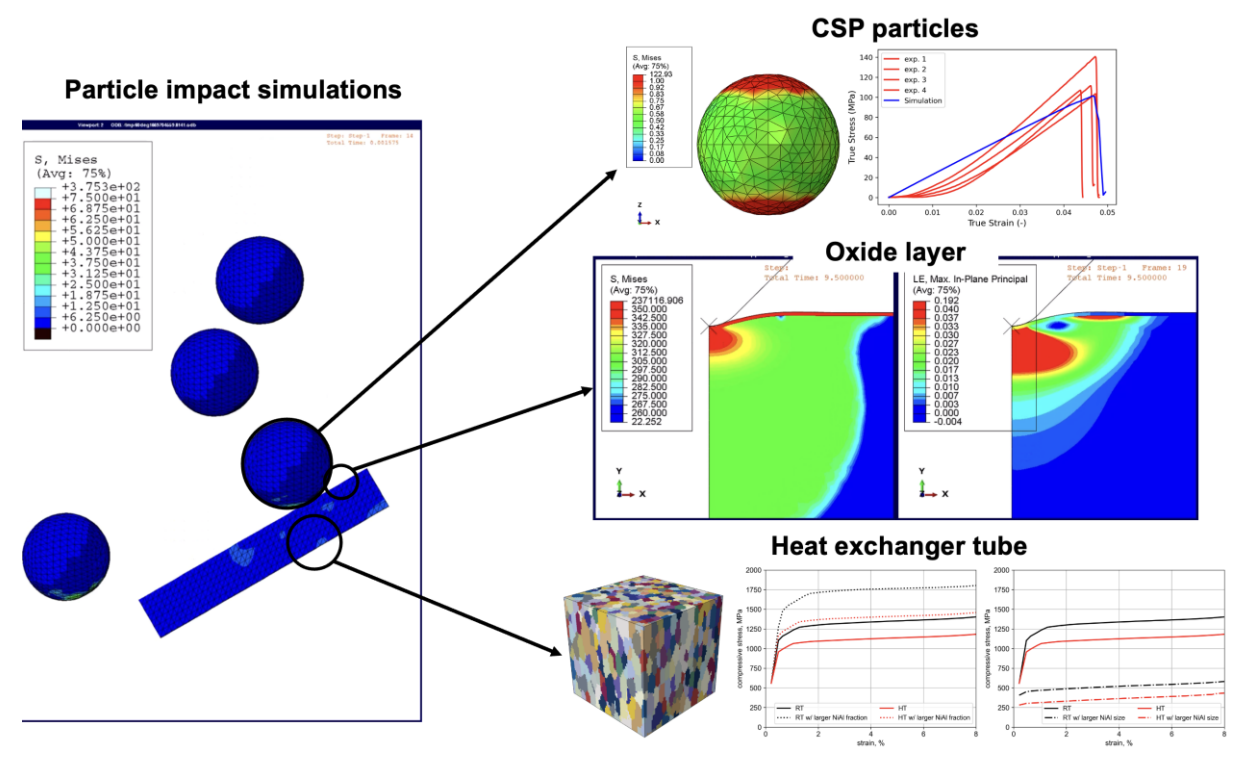


Figure 1: Modeling framework to simulate the degradation in CSP heat exchanger tubes, consisting of particle impact simulations, detailed particle mechanics modeling, response of the oxide layer, and the heat exchanger tube material.

3 BACKGROUND: HIGH TEMPERATURE WEAR IN METALS DUE TO PARTICLE IMPACTS

Particle impacts on metal surfaces result in significant wear, mainly through two mechanisms: **erosion** (Roy, 2006) and **abrasion** (Varga, 2017). Erosion wear occurs when particles strike a metal surface at various angles and velocities, causing material removal through repeated impacts. Abrasion happens when particles slide or roll over the surface, scraping away material. These processes are common in industries with high-speed particles in contact with metal, such as in turbines, pipelines, and mining equipment, leading to reduced durability and efficiency of metal components. We expect that the mechanical wear of the heat exchanger tubes is dominated by abrasive wear mechanism, as the particles are flowing at low speed around the tubes in the operating conditions set in this project.

Erosion Mechanism: Erosion is progressive material loss from repeated particle impacts. Its severity depends on particle size, shape, hardness, impact angle, and velocity:

- Angle of Impact: Impacts at low angles (15-30°) produce more wear in ductile metals, while higher angles (close to 90°) lead to more wear in brittle materials.
- Particle Properties: Hard, sharp particles like sand or minerals cause more severe wear, especially when large or fast-moving.
- Target Material Properties: Softer metals deform under impact, while harder metals resist erosion better.

Abrasion Mechanism: Abrasive wear involves particles sliding along the surface, creating grooves or scratches:

- Two-Body Abrasion: Particles are pressed directly between two surfaces, scoring or plowing through metal.
- Three-Body Abrasion: Particles slide freely, causing less localized but still significant wear.
- Surface Hardness: Abrasion depends on the hardness of the metal relative to particles; softer metals suffer more extensive wear.

Impact of Elevated Temperature: Higher temperatures can worsen wear, as metals soften, reducing hardness and making them more susceptible to particle impacts. In materials like steel, high temperatures weaken microstructures, increasing erosion rates. Some high-temperature alloys resist these effects, retaining hardness under extreme conditions.

Effect of Oxidation: Oxidation is a critical factor in high-temperature wear. Oxide layers can either protect the metal surface or accelerate wear:

- Protective Oxide Layers: Some metals form stable oxides that shield the metal, reducing further erosion or abrasion.
- Brittle Oxide Layers: Brittle oxides can crack and spall under particle impacts, exposing fresh metal and accelerating wear cycles, particularly in metals like iron.

4 MODELING BASED ANALYSIS OF THE DEGRADATION MECHANISMS

In what follows, we carry out a modeling-driven analysis of the degradation of the heat exchanger tubes, based on the experimental investigations carried out previously in Tasks 4.1 and 4.2, to which various simulation techniques are applied to rationalize the results.

4.1 EROSION TEST AT CIEMAT

In the erosion tests carried out by CIEMAT, cylinders were rotated in a container of particles, where the cylinders consisted of state-of-the-art or newly developed heat exchanger materials, and the particles were the state-of-the-art materials. One experiment was performed with Saint-Gobain's bauxite BL16/30 particles, to compare with the newly developed FerOx particles with the same size (590 / 1190 μm). The coatings were tested simultaneously on specimens of P92 and Haynes 282, to study the effect of the coating on metals with FerOx particles. Tests were carried out in air at 700 °C up to 1000 hours with two different rotating speeds corresponding to 5 mm/s and 20 mm/s lineal velocities. Instead of weight loss expected for ideal erosion, the results showed mass gain; based on microstructural analysis, the weight gain seems to be primarily related to deposition of particles on the heat exchanger tube surface, while a secondary effect seems to be oxide scale growth. Due to the mass gain and heavy particle deposition, other experimental data was used to calibrate the modeling approach.

4.2 EROSION-OXIDATION TEST AT FZJ

Three testing facilities were set-up for erosion-oxidation testing at temperatures of 600, 700, and 900 °C in air. The erosion testing was performed in a vertical furnace filled with particles and the specimen holder was rotated at a predefined constant speed. To simulate normal

operating conditions for the particle heat exchanger, the particle velocity was set at 5 mm/s. Additionally, a smaller number of erosion-oxidation testing were performed with a higher particle velocity of 20 mm/s corresponding to maximum possible velocity during plant operation, with more details presented in Deliverable 4.2. For 600 °C and 700 °C, the experimental results indicate minimal mass change when accounting for the oxide film growth. In other words, the oxide films are protective at 600 °C and 700 °C, for typical impact velocities in the operating conditions of 5-20 mm/s. This can be rationalized with a Hertzian contact model, which assumes ideal elastic contact between the particle and oxide film surface. As the deformation depths are below the experimentally observed oxide film thicknesses, we assume that the contact mechanics is dictated by the ceramic particle and the oxide film, which are brittle materials with non-metallic bonding, whose strength is typically limited by the tensile stresses in the material. According to the Hertzian contact model, the only tensile stress states occur at the peripheries of the sphere-plane contact domain (Johnson, 1985); the distribution of these stresses under a 5 mm/s and 20 mm/s impacts are plotted, assuming that all of the impact kinetic energy converts to the elastic mechanical energy. The resulting tensile stress profile is shown in Figure 2, showing that the deformation depths are 1-5 microns at these surfaces.

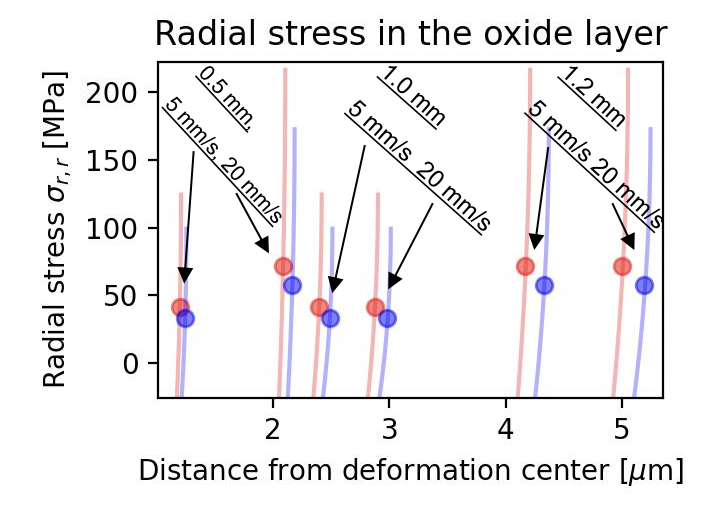


Figure 2: Tensile stresses in a corundum (alumina, Al2O3) oxide layer, showing values below the typical tensile strength of alumina. Red color indicates BL 16/30 (state of the art proppant), and blue indicates the four novel particles developed in WP2 of COMPASsCO2, where the circles indicate the volume-averaged tensile stresses. Three particle diameters are considered: 0.5 mm, 1.0 mm, and 1.2 mm, and two velocities are considered, namely 5 mm/s and 20 mm/s, clustered.

However, as indicated by the experiments at FZJ, the erosion rate increases noticeably at 900 °C for identical particle impact velocities. This is hypothesized to be due to faster and defect-dense oxide films growing at 900 °C compared to 600 °C and 700 °C. Indeed, while the tensile stresses are below 200 MPa and average to approximately 50 MPa in these conditions, the tensile contact stresses can be significantly higher locally if there any microstructural heterogeneities, such as internal pores or large surface roughness or asperities, which often occur due to fast imperfect oxide film growth. These heterogeneities can significantly reduce the critical crack closure stress, i.e. the tensile stress value required to open—not close—a pre-existing microcrack or a new crack. An example of the effect of porosity is shown in Figure 3, showing the difference between a low-porosity (left column) vs. high porosity (right column) oxide microstructure at identical compression levels at different rows; high porosity microstructure leads to higher stress peaks, the middle row shows the microstructures right

before the high porosity microstructure develops a crack, which is shown in the bottom right corner.

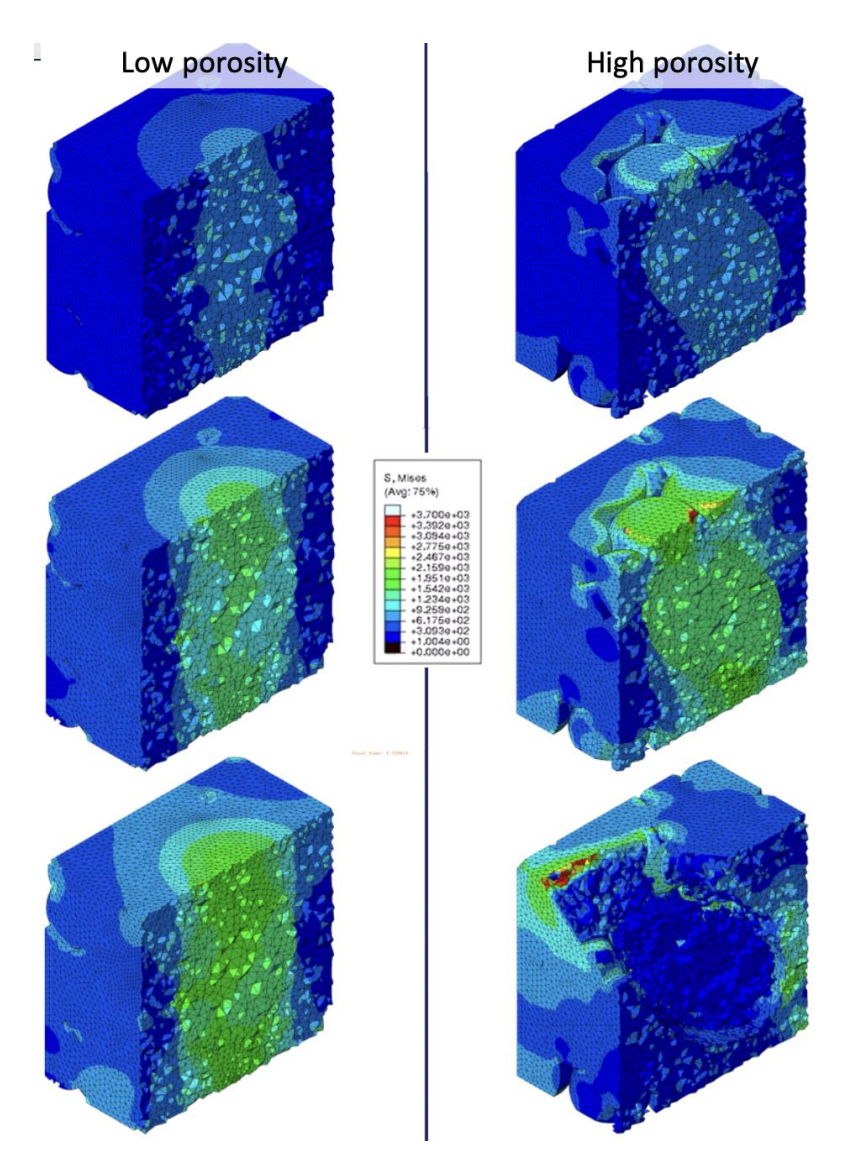
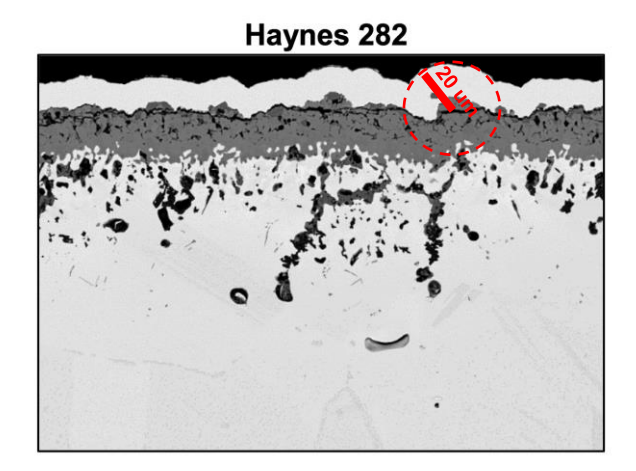


Figure 3: Micromechanical simulations of a representative oxide film microstructures, where left column has a lower volume fraction of porosity, and right column has higher porosity, and each row correspond to a given compression level.

Another source of microstructural heterogeneity is oxide film roughness. Based on experimental images, it is assumed that the oxide film has a characteristic size of approximately 20 microns, estimated from the controlled oxide film analyses in Deliverable D4.1, and the estimation is shown in Figure 4. These types of non-planar asperities are prone to producing stress hot spots.



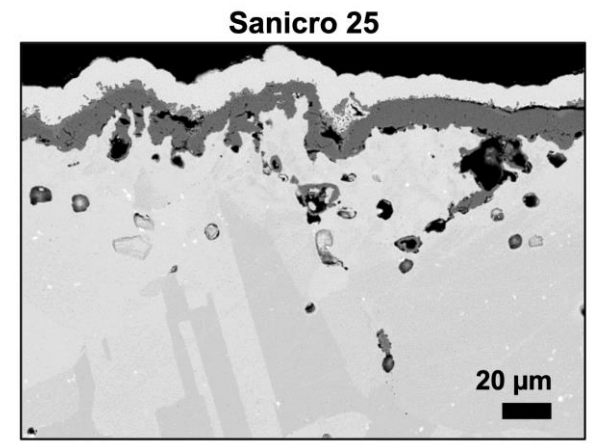


Figure 4: Backscattered electron images, showing the surface oxide layers after 3000 hours of oxidation in 900 C air (original image from Deliverable D4.1). The red circle and line indicate a characteristic surface asperity radius used for contact mechanics analysis.

A more quantitative analysis of this effect based on Hertzian contact mechanics incorporating the effect of asperities was carried out, summarized in Figure 5, where both Al2O3 and Cr2O3 oxide film types are considered. First, the maximum elastic force exerted by the state-of-theart CSP particle (BL 16/30) and a novel generation four (Gen 4) particle are considered, as well as two particle diameters (1 mm and 1.2 mm); additionally, a case where a 1 mm particle impacts head-on to an asperity with radius 20 um (illustrated previously in Figure 4). The results indicate that the asperity leads to significantly higher tensile stresses around the contact, which therefore becomes a likely mechanism of crack initiation in the oxide film. Moreover, these results indicate that between the two considered oxide film types, there is no significant difference in the resulting tensile stresses and the cracking tendency. Note that this does not consider the internal porosity between the two oxide film types, which can differ notably between the two films. Another interesting finding is that the deformation occurs over a relatively small characteristic length scale of 0.1-5 micrometers, which is consistent with the experimental findings in Deliverable D4.2, where it was found that the erosion occurs mostly in the oxide films (and their spallation), and the bulk mechanical properties of the heat exchanger tube material itself seems to have a minor role for the considered impact velocities.

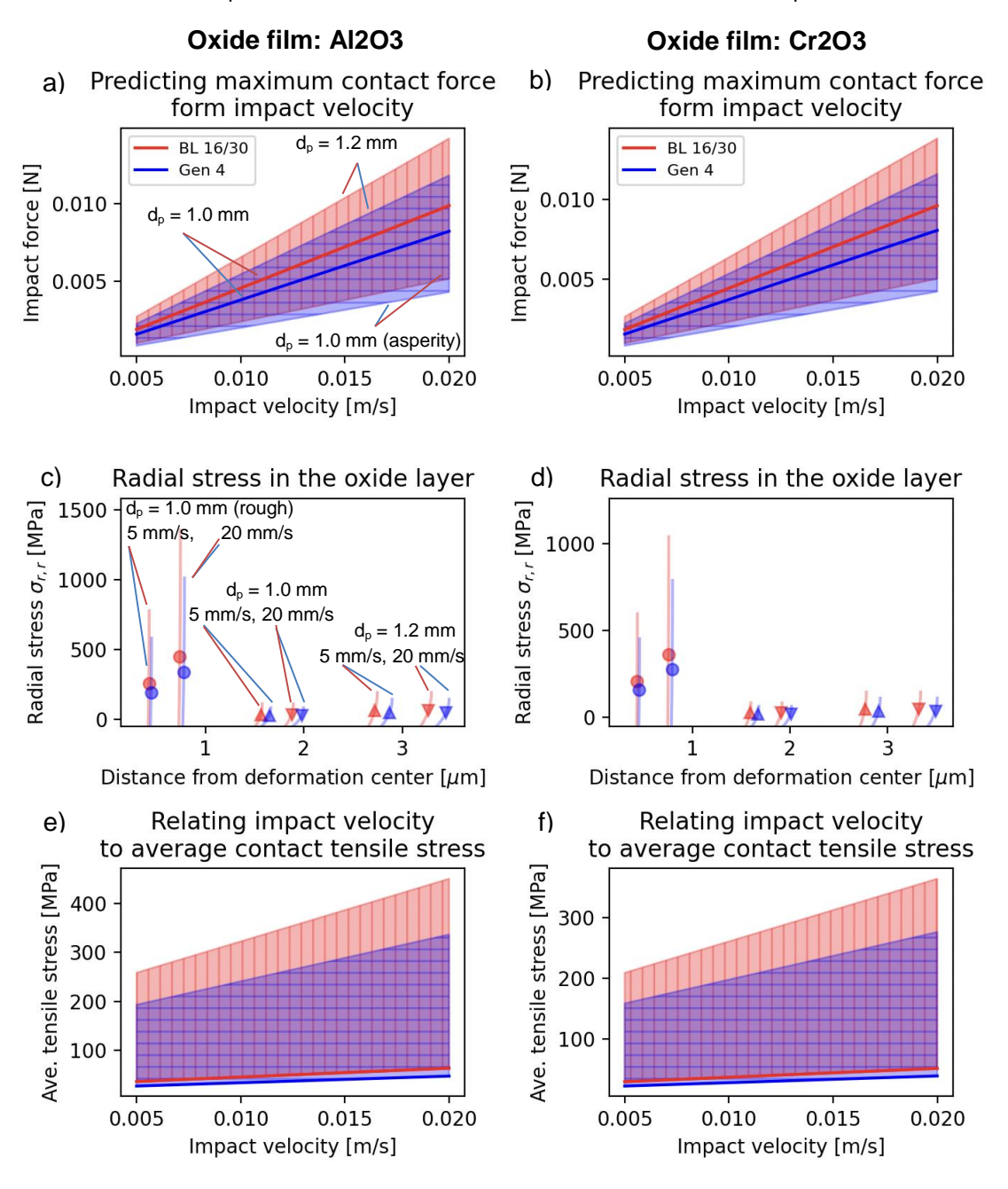


Figure 5: Contact mechanics of Al2O3 and Cr2O3 oxide layers on left and right columns, correspondingly. (a-b) The maximum contact force as a function of impact velocity, where the colors indicate the two particle types, and the spread indicates two particle sizes (1 and 1.2 mm). (c-d) Radial stress state for different particle sizes and impact velocities, where "rough" refers to an impact to an asperity of 20 um radius. (e-f): average tensile stress values as a function of impact velocity, where the high tensile stress values are at 20 um asperities. In all graphs, red color indicates BL 16/30 (state of the art proppant), and blue indicates the novel generation four particles developed in WP2 of COMPASsCO2.

Finally, oxide films can develop notable microstructural stresses due to density changes during the oxide film growths, leading to heterogeneous microstructural stresses, making hot spots of tensile stresses susceptible to crack formation. Note that it is reasonable to assume that the elastic properties of these oxide films do not vary significantly between room temperature and 900 °C (Wang & Fang, 2012).

5 DISCRETE ELEMENT METHOD FOR MODELING PARTICLE DYNAMICS IN THE HEAT EXCHANGER AND LIFETIME ESTIMATION

The backbone of this work is a discrete element method based particle simulation model (Kant & Pitchumani, 2024), which is used to describe the flow of the particles through the heat exchanger tube, and to model the particle collisions on the heat exchanger tube surfaces. The model is based on Lagrangian tracking of particles using an open-source software package called <u>LIGGGHTS</u>. The particle and heat exchanger tube structural material properties (density, size, elastic constants, and hardness) are taken from the literature and the previous deliverables in this project (Deliverables 2.3 and 4.2). The considered geometry is based on the WP5 cold test results, shown in Figure 6a. The distance between the tubes is set so that the horizontal pitch is ten times the particle diameter, i.e. 1 cm.

The representative simulation geometry, shown in Figure 6b, consists of five vertical tube rows, where first, third, and fifth row has two full tubes, and second and fourth row consists of a single full tube in the center, and two halved tubes at the sides; periodic boundary conditions are applied in the vertical directions (along the tube length and along the tube rows), essentially corresponding to infinitely long tubes and infinitely many tubes in each row. Five rows of tubes used as the computational cost increases drastically with the number of tubes considered, and it is feasible to assume that the tubes approach a quasi-steady state behavior as the flow downwards.

A particle diameter of 1 mm was assumed, and the number of particles entering the top part of the system was scaled such that the average mass flow rate per tube top surface area corresponds to the experimental mass flow rate top surface area.

	Density (kg/m³)	Young's modulus (GPa)	Poisson's ratio	Yield strength (MPa)
BL 16/30 particles	3500	319	0.20	-
Gen 4 particles	3300	184	0.15	-
P92 steel	7800	200	0.29	450
Cr-superalloy	7200	279	0.21	700

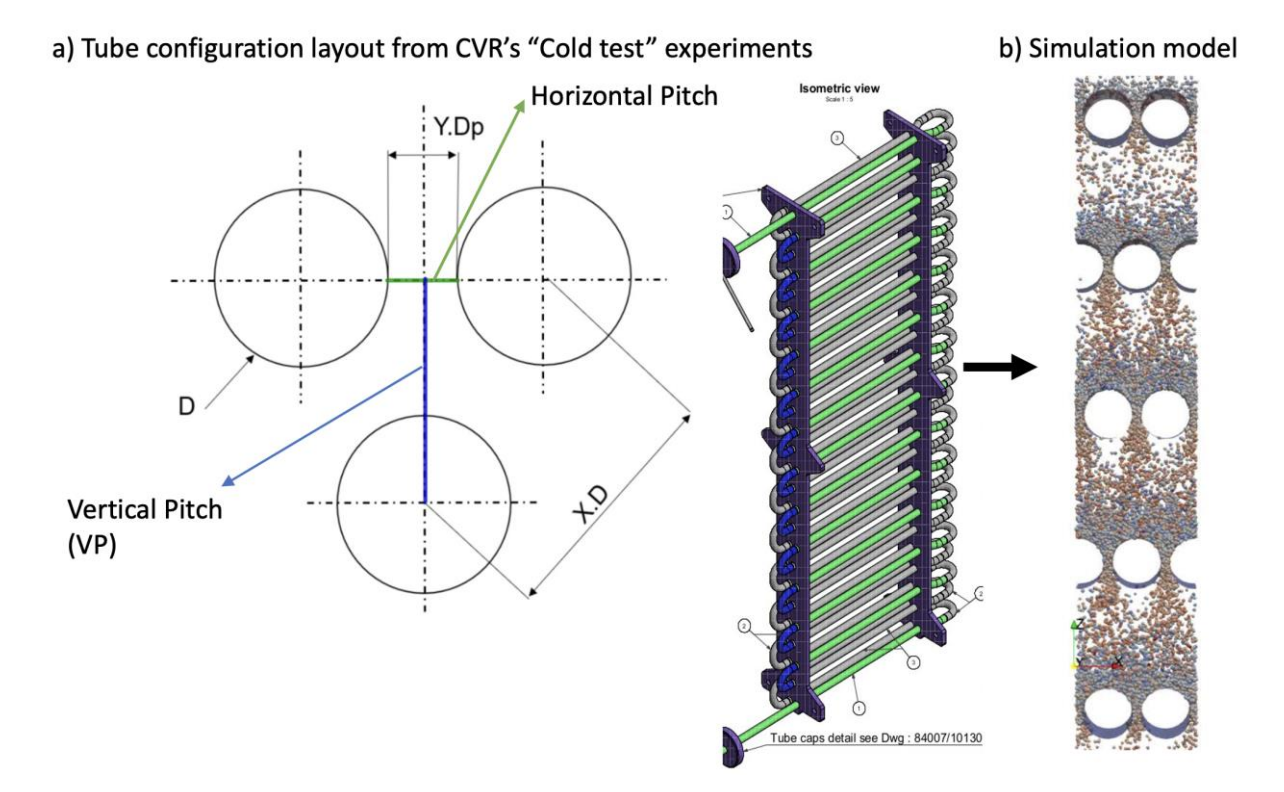


Figure 6: Particle simulation geometry.

The particle impacts are described by a Hertzian contact model, which assumes idealized elastic contact between the particle and the surface, without any off the impact energy being consumed by plastic dissipation. The contact force as a function of time for a single impact is shown in Figure 7 (top), showing that the force obtains a maximum value upon impact, and is reflected with a corresponding force profile away from the surface. The time step size needs to be sufficiently small to smoothly resolve this force profile.

The material wear is described using a Finnie wear model, which assumes that the wear occurs through small incremental removal of material due to impact at an angle, as described by Hertzian contact model of particle-surface interaction. The wear is assumed to accumulate during a single impact before the elastic recoil of the particle starts to move the particle away from the impact surface, i.e. only during the first half of the cumulative wear; the cumulative wear volume during a single impact is shown for a single impact event in in Figure 7 (bottom). It should be noted that the wear volume should be considered a relative quantity at this point, which should be calibrated to experiments.

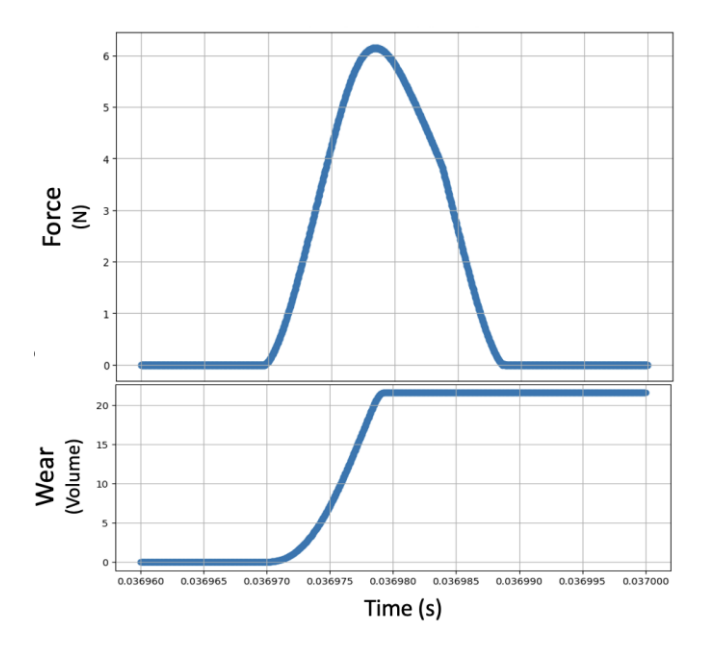


Figure 7: Example of a single particle impact: (top) the force profile according to a Hertzian contact model, (bottom) cumulative wear volume according to the Finnie wear model.

The average velocity as a function of height in the heat exchanger section is shown in Figure 8. The velocity due to gravity between each tube row, and deceleration starts slightly before meeting the next tube row, where the colling and collisions to the tubes slow down the particles. A steady-state behavior is quickly reached, i.e. the same velocity pattern occurs between each tube row.

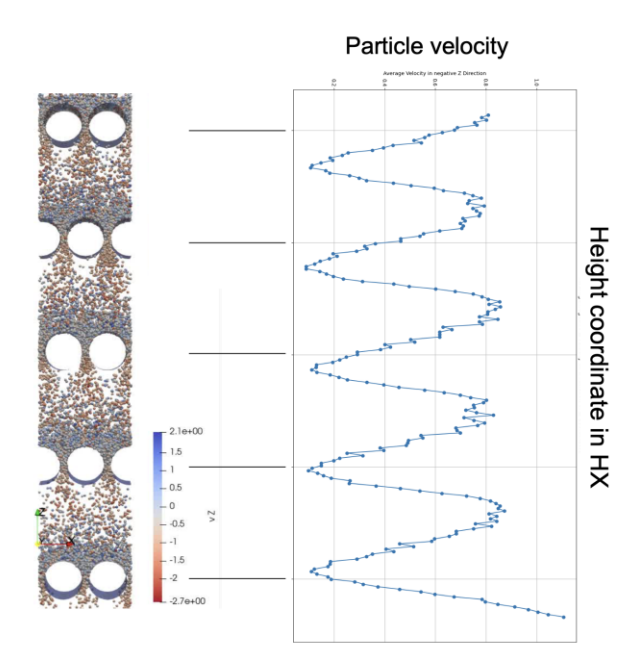


Figure 8: Particle velocity as a function of height in the heat exchanger system. It can be seen that the velocity due to gravity between each tube row, and deceleration starts slightly before meeting the next tube row, where the colling and collisions to the tubes slow down the particles. A steady-state behavior is quickly reached, i.e. the same velocity pattern occurs between each tube row.

The Lagrangian particle simulations discussed in this section have a high computational cost. This is due to the large number of particles in the simulation box to have a representative geometrical section of the full heat exchanger domain. In addition, to fully resolve the Hertzian contact events in time, the simulations are restricted to a relatively small time step. With the current set-up, a typical simulation runs approximately one week, using 120 processors on a supercomputer. Following key measures in the simulations, such as the velocity distributions and local wear rate, we believe that approximately 10 seconds are needed to reach a representative "steady-state" flow condition in the simulated heat exchanger; longer simulation times show a rather linear increase in the wear volume and particle velocity distributions, with stochastic fluctuations visible.

The wear in the simulation system during a 13.5 second simulation is shown in Figure 9. The wear tends to accumulate to the tube top diagonals and not in the tube top center (zenith). The wear is stochastically distributed on the tube surface based on the particle impacts, so there is a rugged distribution of wear accumulating to the tube surface; the 95 percentile of the wear volumes are shown in Figure 9 c, where each line is colored by their tube height coordinate: yellow lines are at the top and therefore start to experience wear before the bottom row of tubes (dark blue). The wear rate (wear volume per time) is very similar for each tube surface, and the differences are roughly due to the distances from the tube surface. The wear starts to reach a steady-state regime after approximately 6 seconds. In Figure 9 d, the zoom-in is shown for the cumulative wear volume; as expected, the wear lowest in the bottom level tube arrays, which have experienced the least amount of particle impacts during a continuous particle flow simulation. Moreover, the dashed lines show the left-side tubes, and solid lines are the right-side tubes, showing that the difference between the sides are negligible.

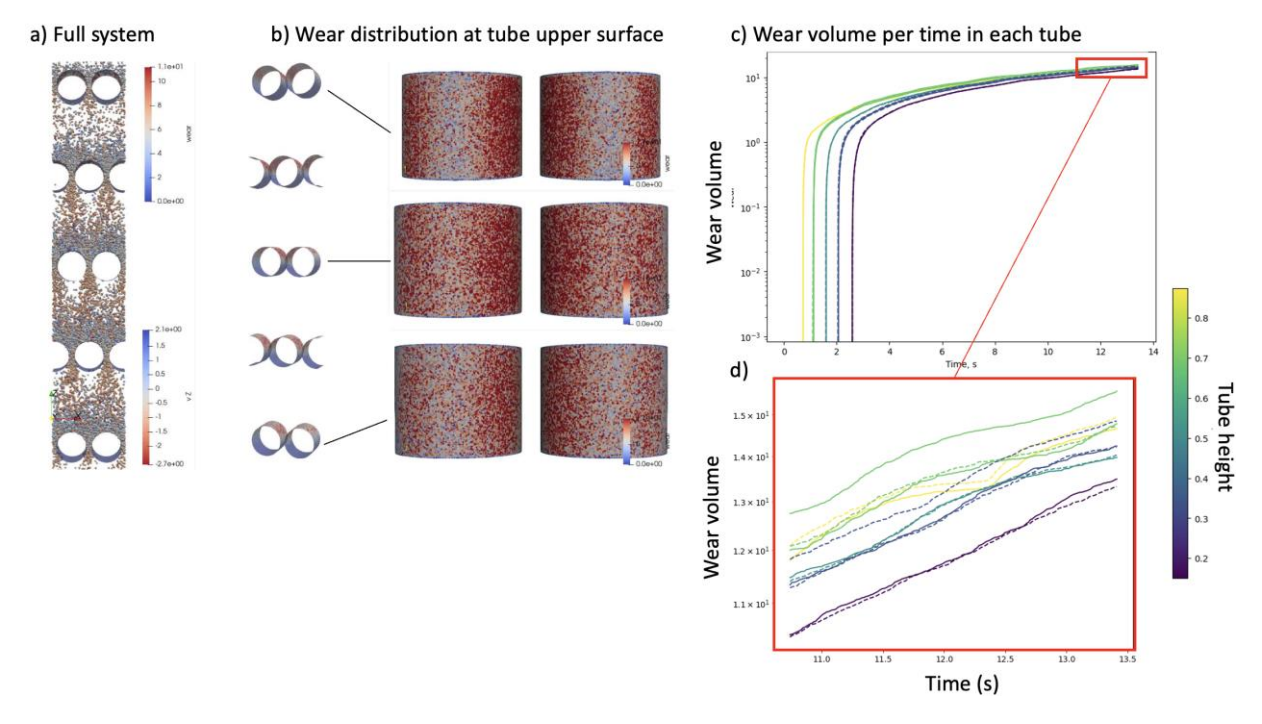


Figure 9: Wear in the heat exchanger system during a 13 second simulation, showing (a) full simulation system, (b) distribution of wear at three tube rows on top side, (c) 95 percentile of wear in each tube colored by tube height coordinate, and (d) zoom-in to the end of the simulation time.

The comparison between two different vertical pitch to tube diameter ratios are considered in Figure 10, where the left side is the reference case, and right side is a denser tube set-up; the

bottom panels show the tube geometry, distribution of particles and wear, and the top panels show the force and wear per tube row. For the denser tube set-up (right side), the forces are orders of magnitude smaller, and importantly, the wear is high on the upper-most tube arrays, after which the particle flow slows down considerably, leading to lower wear volumes; for the reference case (left-side set-up), the wear volume also decreases, but to a lesser degree.

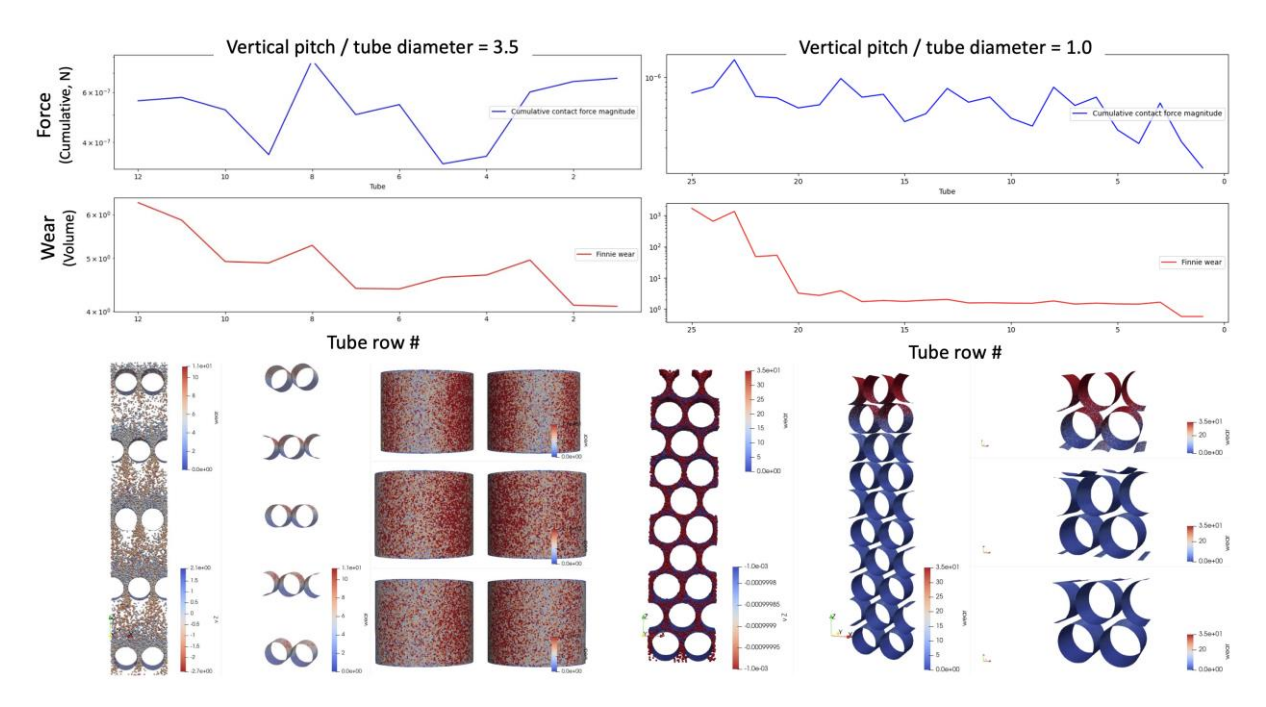


Figure 10: Comparison of force and wear distribution with a looser (left) and denser (right) arrangement of tubes. The wear volume decreases quickly for the denser tube arrangement, which can be attributed to the decrease of particle velocity.

It should be noted that at this point, only the relative wear volumes should be considered; the absolute wear volume comparison require calibration to experiments, which will be carried out as follows.

6 CALIBRATION OF THE LIFETIME ESTIMATION MODEL

In the erosion-oxidation wear tests carried out by FZJ (Deliverable D4.2), it was concluded that the wear occurred exclusively on the oxide films. Therefore, our subsequent analysis focuses on the wear in the oxide films. For now, we exclude the Sanicro 25 analysis, where particle deposition occurs, as this complicates the analysis notably. Based on the 1000 h tests, the linearized average wear rate for IN740 is (5.4-1.6) mg/cm² / 800 h ~ 0.520 g/m² / year. Assuming IN740 density of 8.05e3 kg/m³, the cumulative wear in 10 years is approximately 0.52 mm; in COMPASsCO2, the heat exchanger tube thickness is ~ 2.5 mm; this implies that on average, 20% of the full tube thickness, which also means that, considering the potential localization of plastic deformation, cracking, and wear, it is very likely that locally a structural failure occurs in the tubes during a 10 year lifespan. We calibrate the lifetime estimation model to the IN740 wear volume, and the resulting wear evolution is shown in Figure 11, where the first two panels show the wear versus time versus tube array row number (#) in the discrete element simulations of wear. Linear fit is performed for the quasi-steady state wear accumulation, starting from ~ 5 seconds to the end of the simulation, i.e. 13.5 seconds, as shown in Figure 11 (middle panel). The same wear accumulation is expected to occur over time, and the accumulated wear is calibrated to the FZJ IN740 wear test after 1000 hours (right panel in Figure 11). By using the IN740 density, the accumulated wear (kg/m²) was converted to wear depth (mm).

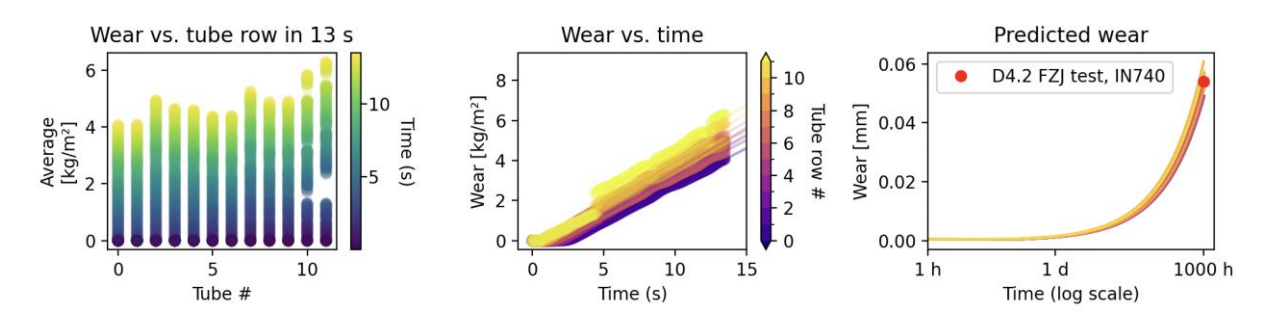


Figure 11: Calibration of the lifetime estimation model to FZJ wear test (from deliverable D4.2), showing the average wear per tube row (left), wear versus time (middle), and the calibrated wear rate up to the 1000 h experiments.

One advantage of discrete element simulations is that statistics of the wear can be obtained. In this case, for the accumulated wear, the focus is on the median (typical value) and 95 percentile, shown as their own rows in Figure 12. Interestingly, the median varies much more than the extreme, indicating that the behavior is more predictable, as it is likely that the extreme events are what lead to localization of deformation and potential catastrophic failure.

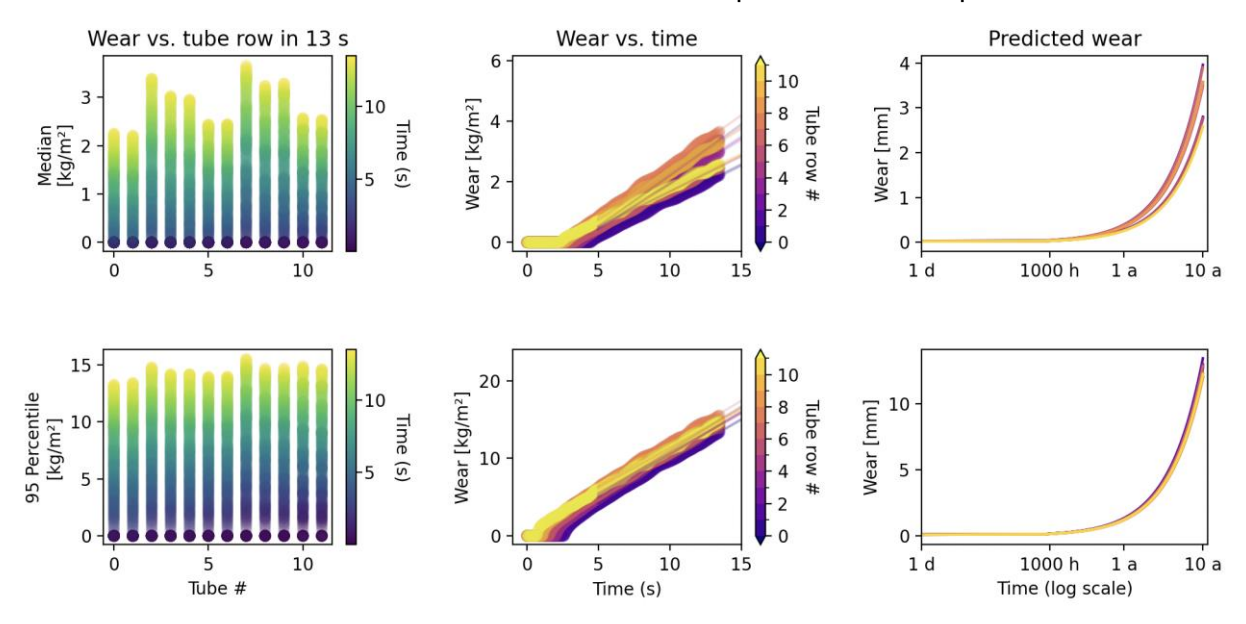


Figure 12: Wear prediction for IN740 for 10 years in terms of the median (typical) and 95 percentile (extreme), calibrated to the experimental wear tests.

Finally, Figure 13 shows the wear depth after 10 years of operation in IN740, Haynes 282, and Cr-superalloy, as predicted by the modeling approach. This shows that the wear in IN740 and Haynes 282 are very similar, whereas the Cr-superalloy shows a slightly higher wear volume. It should be noted that for conclusive results, more careful wear tests should be carried out for Cr-superalloy, which is expected to behave in a qualitatively different manner compared to the superalloys (Ma, 2023).

Figure 13: Wear depth prediction for IN740, Haynes 282, and Cr-superalloy for ten years.

7 CONCLUSIONS

The modeling-based analysis is applied to the heat exchanger tube materials to better understand and predict the degradation behavior. The main conclusions are as follows.

7.1 DEGRADATION MECHANISM ANALYSIS

The contact mechanics modeling verifies that once an oxide layer forms, the particle contact and the associated stress-strain distribution is highly localized within several micrometers area, verifying that indeed, the particles are likely interact mostly with the small-scale oxide layers present on the heat exchanger material surfaces, which are known to form relatively quickly based on the D4.1 and D4.2 experiments. This conclusion supports the experimental findings of FZJ D4.2 erosion-corrosion tests, which suggests that the wear occurs mainly as detachment or spallation of the corrosion layers. Moreover, due to the brittle nature of the particles and the corrosion oxide layers, it is highly unlikely that the facture initiates due to an ideal spherical contact between the proppant and the corrosion oxide surface; instead, any heterogeneities, likely surface asperities or internal pores, are likely to initiate the fracture. Our results also indicate that the fracture initiation does not differ significantly across different particles or corrosion oxide chemistries in terms of their bulk material properties; however, the porosity and surface morphology of the oxide layers and the particles are likely to determine how large tensile stresses emerge in the contact region. A more detailed analysis of the oxide layer contact mechanics would require careful nanoindentation testing, and 3D tomographic imaging of the oxide microstructures to reveal their pore structures, as well as the statistics of their surface asperities.

7.2 LIFETIME ESTIMATION

A major effort in Task 3 was the establishment of a discrete element method-based particle simulation framework, which allowed us to simulate the particle flow in the heat exchanger tube arrangement, and importantly, evaluation of the contact forces and wear volumes using a phenomenological Finnie wear model. This approach allows us to identify that in the heat exchanger surface, detrimental collisions are most likely to occur at the top, but not in the middle of the tube upper surface, but closer to the sides. We can also analyze the statistics of the collisions; in this case, we considered the median (typical) and 95 percentile (extreme) accumulated wear. Our simulations indicate that the median wear varies significantly across notably, roughly 20-40 %, between tube arrays, whereas the extreme collision events are more uniformly distributed between the tube arrays. Due to the high complexity of the wear and corrosion at elevated temperatures in operating conditions, we calibrated the lifetime

estimation model to experimental data performed by FZJ in D4.2, to extrapolate the lifetime of the tubes up to ten years of service.

REFERENCES

- Johnson, K. (1985). Contact Mechanics. Cambridge University Press.
- Kant, & Pitchumani. (2024). Erosion wear analysis of heat exchange surfaces in a falling particle-based concentrating solar power system. *Solar Energy Materials and Solar Cells*, 112629.
- Ma, K. (2023). Chromium-based bcc-superalloys strengthened by iron supplements. *Acta materialia*, 119183.
- Roy, M. (2006). Elevated temperature erosive wear of metallic materials. *Journal of Physics D: Applied Physics*, 39 (101).
- Varga. (2017). High temperature abrasive wear of metallic materials. Wear, 443-451 (15).
- Wang, Y., & Fang, H. (2012). First-principles lattice dynamics, thermodynamics, and elasticity of Cr2O3. *Surface Science*, 1422-1425.